remote sensing

MDPI

Article

The VIIRS Day/Night Band: A Flicker Meter in Space?

Christopher D. Elvidge [1,*], Mikhail Zhizhin [1,2], David Keith [3], Steven D. Miller [4], Feng Chi Hsu [1], Tilottama Ghosh [1], Sharolyn J. Anderson [5], Christian K. Monrad [6], Morgan Bazilian [7], Jay Taneja [8], Paul C. Sutton [9], John Barentine [10], William S. Kowalik [11], Christopher C. M. Kyba [12], Dee W. Pack [13] and Dorit Hammerling [14]

1 Earth Observation Group, Payne Institute for Public Policy, Colorado School of Mines, Golden, CO 80401, USA; mzhizhin@mines.edu (M.Z.); fengchihsu@mines.edu (F.C.H.); tghosh@mines.edu (T.G.)
2 Russian Space Research Institute, Moscow 117997, Russia
3 WSP Global Inc., Montreal, QC H3H 1P9, Canada; david.keith@wsp.com
4 Cooperative Institute on Research on the Atmosphere, Colorado State University, Fort Collins, CO 80521, USA; steven.miller@colostate.edu
5 National Park Service—Natural Sounds and Night Skies Team, Fort Collins, CO 80525, USA; sharolyn_anderson@nps.gov
6 Monrad Engineering, Inc., Tucson, AZ 85719, USA; chrismonrad@monradengineeringinc.com
7 Payne Institute for Public Policy, Colorado School of Mines, Golden, CO 80401, USA; mbazilian@mines.edu
8 Electrical and Computer Engineering, University of Massachusetts, Amherst, MA 01003, USA; jtaneja@umass.edu
9 Department of Geography, University of Denver, Denver, CO 80210, USA; paul.sutton@du.edu
10 Dark Sky Consulting, LLC, Tucson, AZ 85730, USA; john@darkskyconsulting.com
11 Oregon Chapter of the International Dark-Sky Association, Bend, OR 97709, USA; wsk412@sbcglobal.net
12 GFZ German Research Centre for Geosciences, Telegrafenberg, 14473 Potsdam, Germany; kyba@gfz-potsdam.de
13 Remote Sensing Department, Aerospace Corporation, El Segundo, CA 90245, USA; dee.w.pack@aero.org
14 Department of Applied Mathematics and Statistics, Colorado School of Mines, Golden, CO 80401, USA; hammerling@mines.edu
* Correspondence: celvidge@mines.edu

check for updates

Citation: Elvidge, C.D.; Zhizhin, M.; Keith, D.; Miller, S.D.; Hsu, F.C.; Ghosh, T.; Anderson, S.J.; Monrad, C.K.; Bazilian, M.; Taneja, J.; et al. The VIIRS Day/Night Band: A Flicker Meter in Space? *Remote Sens.* **2022**, *14*, 1316. https://doi.org/10.3390/rs14061316

Academic Editors: Ran Goldblatt, Steven Louis Rubinyi and Hogeun Park

Received: 17 January 2022
Accepted: 4 March 2022
Published: 9 March 2022

Publisher's Note: MDPI stays neutral with regard to jurisdictional claims in published maps and institutional affiliations.

Abstract: The VIIRS day/night band (DNB) high gain stage (HGS) pixel effective dwell time is in the range of 2–3 milliseconds (ms), which is about one third of the flicker cycle present in lighting powered by alternating current. Thus, if flicker is present, it induces random fluctuations in nightly DNB radiances. This results in increased variance in DNB temporal profiles. A survey of flicker characteristics conducted with high-speed camera data collected on a wide range of individual luminaires found that the flicker is most pronounced in high-intensity discharge (HID) lamps, such as high- and low-pressure sodium and metal halides. Flicker is muted, but detectable, in incandescent luminaires. Modern light-emitting diodes (LEDs) and fluorescent lights are often nearly flicker-free, thanks to high-quality voltage smoothing. DNB pixel footprints are about half a square kilometer and can contain vast numbers of individual luminaires, some of which flicker, while others do not. If many of the flickering lights are drawing from a common AC supplier, the flicker can be synchronized and leave an imprint on the DNB temporal profile. In contrast, multiple power supplies will throw the flickering out of synchronization, resulting in a cacophony with less radiance fluctuation. The examination of DNB temporal profiles for locations before and after the conversion of high-intensity discharge (HID) to LED streetlight conversions shows a reduction in the index of dispersion, calculated by dividing the annual variance by the mean. There are a number of variables that contribute to radiance variations in the VIIRS DNB, including the view angle, cloud optical thickness, atmospheric variability, snow cover, lunar illuminance, and the compilation of temporal profiles using pixels whose footprints are not perfectly aligned. It makes sense to adjust the DNB radiance for as many of these extraneous effects as possible. However, none of these adjustments will reduce the radiance instability introduced by flicker. Because flicker is known to affect organisms, including humans, the development of methods to detect and rate the strength of flickering from space will open up new areas of research on the biologic impacts of artificial lighting. Over time, there is a trend towards the reduction of flicker in outdoor lighting through the replacement of HID with

low-flicker LED sources. This study indicates that the effects of LED conversions on the brightness and steadiness of outdoor lighting can be analyzed with VIIRS DNB temporal profiles.

Keywords: VIIRS; DNB; flicker; artificial lighting

1. Introduction

A "flicker meter" is a device capable of recording and characterizing the brightness cycling of lighting powered by alternating current (AC) [1]. In AC, the electrons flow back and forth at a well-regulated frequency. Mass distribution power supplies around the world operate at either 50 or 60 Hertz (cycles per second). AC is frequently converted to direct current (DC) to provide a more stable power supply to devices and appliances, in a process called "rectification". The full-wave rectification (Figure 1) of a 60 Hz source results in lights flickering at 120 Hz, but with half the amplitude of the original alternating current. Further reductions in the amplitude of flicker can be achieved by voltage smoothing with capacitors (common in fluorescent lights) and "constant current" drivers [2] used to power large-wattage LED sources (Figure 1).

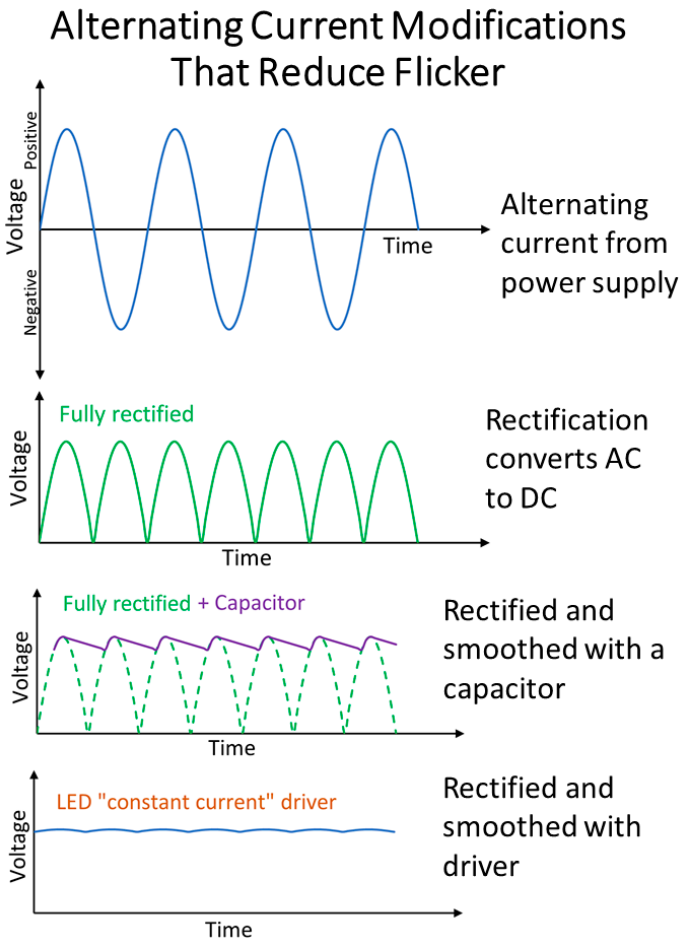

Figure 1. Voltage versus time patterns for alternating current, full-wave rectification, smoothing accomplished with a capacitor, and LED "constant-current".

The "critical flicker frequency" [3] or frame rate of human vision is variable but is placed in the range of 3 to 70 Hz [4]. It is well established that lighting flicker within the range of visual perception can induce neurological symptoms like headaches, loss of attention and visual acuity, irritability, and in some cases, epileptic seizures [5,6]. Most

modern luminaires have been engineered to minimize flicker below 50 Hz. However, many light sources flicker in the range of 100 to 120 Hz, which is above the range of conscious perception to the human eye.

The effects of 100–120 Hz flicker on humans remains an active research area. One recent study found that humans are subtly affected by lighting flicker up to 500 Hz [7]. Exposure to flicker at rates above 70 Hz for long periods of time can result in neurological symptoms such as induced photosensitivity [8], chronic migraine and fatigue, and anxiety, depression, and irritability [9]. There is a growing body of evidence that lighting flicker adversely affects other organisms [10]. The satellite detection and characterization of flickering lights would open up a range of new research opportunities in the field of anthropogenic impacts on many organisms, including humans.

To fully resolve the flicker pattern requires temporal sampling that is nearly ten times shorter than the flicker rate being measured [11]. Thus, for 120 Hz flickering, the flicker meter, as one of its design criteria, should measure the brightness of the light at 1200 Hz. This corresponds to a sampling rate of 8.3×10^{-4} seconds (s). According to Table 3.3-6 on page 52 of the VIIRS geolocation Algorithm Theoretical Basis Document (ATBD) [12], the VIIRS DNB pixel dwell time ranges from 2.53×10^{-4} s at nadir to 4.22×10^{-5} s at the edge of scan. If this is true, the DNB pixel dwell time is shorter than the minimum acceptable sampling interval recommended for characterizing 120 Hz flickering.

The standard flicker meter collects many cycles in a single collection session to fully resolve the temporal pattern of the flicker of an individual light. In contrast, the VIIRS DNB collects once or twice per night across many years. At 742 m on a side, DNB pixels may contain hundreds of individual lights of various types. Radiance calibrated VIIRS DNB temporal profiles can be assembled, filtered to remove flawed data, adjusted for a range of radiance contributors such as moonlight, and analyzed for events such as power outages or cycling. Is it also possible to discern differences in AC flicker patterns within VIIRS temporal profiles?

In this paper, we clarify the VIIRS DNB pixel dwell time specifically for the nighttime collection mode, define the flicker characteristics for the major types of lighting, and examine VIIRS DNB temporal profiles for evidence of flicker.

2. Materials and Methods

2.1. Calculation of DNB Pixel Dwell Times for High Gain Stage Data

The VIIRS DNB focal plane assembly contains four detector arrays (Figure 2), which are swept across the earth to construct 16 lines of DNB pixels on each scan [12]. DNB pixel footprints on the earth's surface are maintained at almost 742 m on a side from nadir to edge of scan by the onboard aggregation of different numbers of adjacent detectors in both the track and scan directions. The number of detectors aggregated is largest at nadir and drops gradually, moving toward the edge of scan in fixed patterns, referred to as aggregation zones. Pixels from the first aggregation zone, near nadir, are constructed using 66 detectors in the scan direction and 42 in the track direction (Figure 2). In aggregation zone 32—at the edge of scan—pixels are formed using 11 detectors in the scan direction and 20 detectors in the track direction (Figure 2). All four DNB detector arrays have 672 detectors in the track direction to afford the exact number of detectors required to form the aggregation zone 1 pixels ($16 \times 42 = 672$). Each of the DNB detector arrays are 672 detectors high but vary in width based on the amplification requirements to image clouds from daylit to moonlit conditions. Under daylit conditions, no amplification is required, so the low gain stage (LGS) focal plane array is only one detector wide. The signal amplification is achieved by accumulating charge from multiple samples of the same sub-pixels—a process known as time delay and integration (TDI). The medium gain stage (MGS), designed for cloud imaging in the transition from day to night at dawn and dusk, has three parallel rows of detectors for collecting data with a TDI of three. The highest level of signal amplification comes from the high gain stage (HGS), which is 250 detectors wide. The HGS arrays collect

data with a TDI of 250. The HGS is designed to collect at night and is responsible for recording radiances from electric lighting.

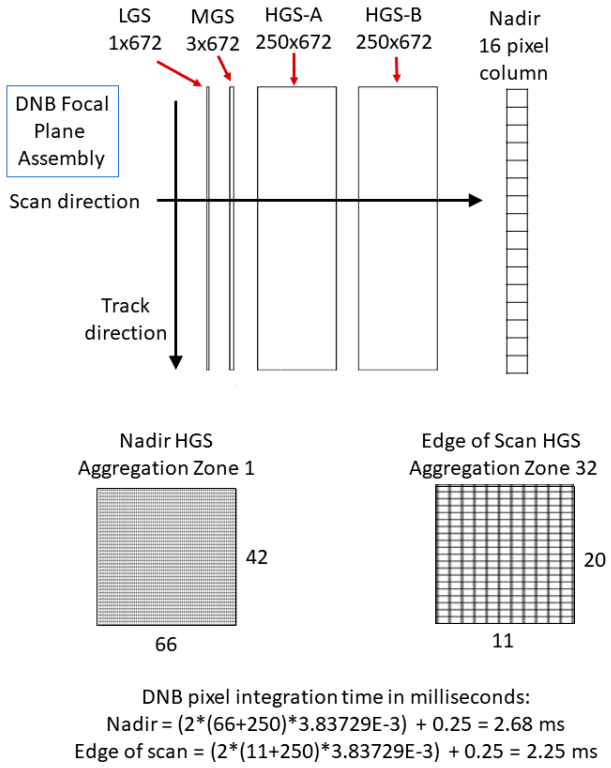

Figure 2. Schematic showing the four DNB detector arrays and the aggregation of charge from variably sized blocks of detectors to maintain near-constant 742 × 742 m ground footprints from nadir to edge of scan. LGS = low gain stage, optimized for daytime collections. MGS = medium gain stage, optimized for collection across the terminator during the transition from day to night. HGS = high gain stage, optimized for nighttime imaging.

There are two HGS detector arrays, referred to as HGS-A and HGS-B. This redundancy is designed to filter out high energy particle detections, which are common when the spacecraft flies through the South Atlantic Anomaly (SAA), which is centered near Rio de Janeiro, Brazil. An onboard algorithm compares the signal from the same ground pixel from HGS-A and HGS-B. If there is a large difference between the two, the brighter pixel is dropped, and the pixel's recorded radiance only comes from one of the two HGS detector arrays. If the difference is modest, the two HGS signals are averaged.

The detector array sampling rate of the DNB is 260.6 KHz [12], corresponding to 3.83729×10^{-3} milliseconds (ms) per detector. The DNB integration table in the ATBD [12] calculates DNB pixel collection times by multiplying the subpixels in the scan direction by 3.83729×10^{-3} s. These numbers are correct for the LGS, which has no TDI, and accumulating all 66 along-scan detectors (aggregation zone 1) yields 2.53×10^{-4} s. To add in the TDI to the DNB pixel HGS collection time, an oversample factor of 250 is applied to each detector in the along-scan direction (Figure 3). Thus, at nadir, the HGS-A pixel collection time is (66 + 250) times 3.83729×10^{-3} ms = 1.213 ms. To this, we add the gap time between HGS-A and HGS-B, which is estimated to be 0.25 ms, and then add the time required to collect HGS-B, which is the same (1.213 ms) as HGS-A. Thus, the total integration time for a HGS DNB pixel at nadir is 2.67 ms, while for aggregation zone 32, it is 2.29 ms.

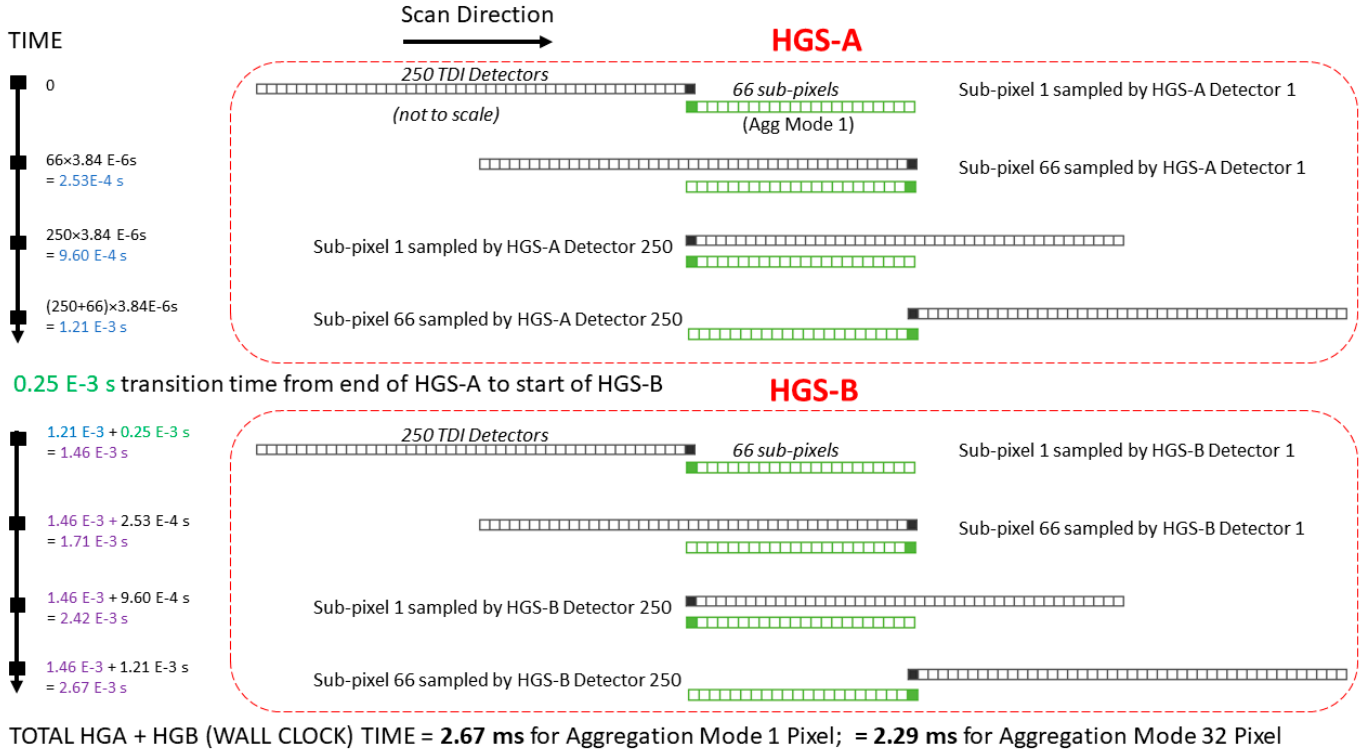

Figure 3. Timeline for the VIIRS DNB HGS pixel aggregation.

It is important to note that the four DNB detector arrays collect photons and accumulate charge continuously during the scan across the earth, but that the zone of active pixel formation gradually tapers from nadir to edge of scan (Figure 4) to maintain the 742 m DNB pixel size. At nadir, all 672 detectors are read out to form pixels. At the edge of scan, the number of detectors actively involved in pixel formation drops to 320. Similar tapering occurs on the LGS and MGS arrays. At any one instant, the HGS detector arrays collect data for a number for DNB pixels. This number can be calculated as 250 divided by the number of sub-pixels in the scan direction. At nadir, this is 250/66 = 2.79 pixels and at the edge of scan, 250/11 = 22.72 pixels. Onboard, the DNB evaluates the pixel voltages from HGS, MGS, and LGS to record the highest unsaturated voltage. Pixels with bright surface lighting will have a usable signal in the HGS but remain undetectable in the MGS and LGS. Conversely, daylit clouds will have a usable voltage from the LGS, while the HGS signal will be saturated. This arrangement makes it possible for the DNB to instantly adjust to abrupt changes in brightness, such as transits across the dawn–dusk lines.

As an interesting side note, we expected that the HGS noise filtering would eliminate the South Atlantic Anomaly high-energy particle detections commonly found in the low-light imaging data collected by the VIIRS predecessor: the U.S. Air Force Defense Meteorological Satellite Program (DMSP) Operational Linescan System (OLS). The SAA-affected pixels have high radiance levels in unexpected places, such as the Atlantic Ocean between Africa and South America. Their numbers appear unchanged between OLS and VIIRS. Several years ago, we conducted an experiment where HGS-A and HGS-B were brought down intact from the satellite along with the normal DNB data stream using one of the VIIRS calibration modes. The HGS-A and HGS-B could not be brought down simultaneously, so they were brought down in alternating granules collected over the Atlantic Ocean south of the equator—a zone famous for SAA detections. We found that SAA hits in both the HGS-A and HGS-B, but these were absent from the normal DNB data. However, the normal DNB data from those granules had a different set of SAA detection pixels. Our conclusion was that the HGS noise filtering is working as designed. Therefore,

the SAA detections present in the DNB data stream must be coming from the MGS or LGS, which lack the noise filtering.

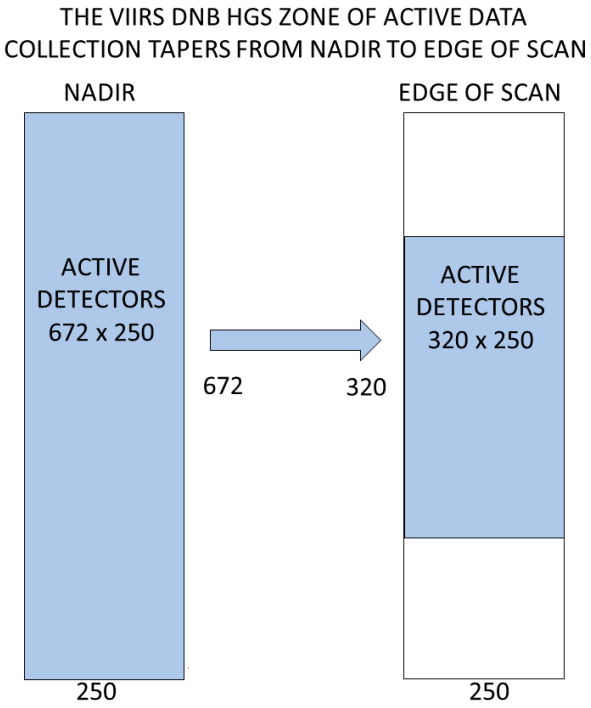

Figure 4. The active zone of DNB pixel formation tapers from 672 detectors in the track direction at nadir to 320 detectors at the edge of scan.

2.2. Collection of High-Speed Camera Data of Individual Luminaires

High-speed camera (HSC) data and spectral signatures were collected for the set of individual luminaires listed in Table 1. Most of the data collections were made with a Sony Cyber-Shot DSC-RX100 V 20.1 operated at 1000 frames per second. A second camera was used to collect data from a hovering DJI Mavic Air 2S drone in Moscow using the built-in camera running at 120 frames per second. We also experimented with the collection of flicker data on the panoramic views of city lights with a night vision photomultiplier tube (PMT) adapter (generation 3+ auto-gated white phosphor AGM PVS-14) replacing the fore optics of the Sony camera. Both the original Sony camera and PMT-equipped Sony camera were tested for the presence of flicker or other aberrations with high-speed camera data collected on the moon as a flicker-free light source in the night sky.

The MP4 files collected of the luminaires are available via the links listed in the supplemental material. Temporal profiles were produced from rectangular subsets of the video frames centered on the light sources. A brightness threshold was applied to each frame to minimize the inclusion of background into the temporal profiles, which are also available in the supplemental material.

Luminaire spectra were collected with a BWTek BRC112E spectrometer covering the 400 to 1000 nanometer range. The spectrometer was mounted to record the luminaires' reflectance from a Spectralon panel. Like fingerprints, the spectra were used to confirm the lighting types based on previously published spectral signatures of lights [13].

Table 1. Individual luminaires measured.

Luminaire Type	Designation	Sample	Manufacturer	Model	Wattage
Metal Halide	Ceramic Metal Halide	C0009	Sylvania	MetalARC Mp 100/U/MED	100
	Metal Halide	C0012	EMCO Lighting	ERA20-3H SO-89193	175
	Metal Halide	C0015	Philips	MP400/BU/PS Kr85	400
	Metal Halide RAB	C0016	RAB	RAB LMH250PS	250
High Pressure Sodium	HPS	C0017	Sylvania	LU150/55/ECO	175
	HPS	C0041	General Electric	Lucalox	100
Low Pressure Sodium	LPS	C0007	Osram	N068 80X Great Britain	18
Fluorescent	4 foot tube pair	C0006	Philips	Alto F40T/C50 Sumpreme	40
	Fluorescent ceiling	C0035	Philips	Alto-II F32T8/Tl841 800 series	32
	Compact Fluorescent	C0028	BFLG	13	13
	Compact Fluorescent	C0031	Greenlight	13W/ELS-M/1	13
	Compact Fluorescent	C0032	TCP	ESN11	11
Incandescent	Incandescent	C0014			
	Incandescent	C0027	Sylvania	Capsylite FL-tugsten-halogen	45
	Incandescent	C0034	Soft White		60
LED	LED	C0018	PLT Solutions	PLT-11557	300
	LED 4000 K	C0020	LeoTEK	Beta	100
	LED 3000 K	C0022	LeoTEK	Beta	100
	LED	C0026	Lithonia	DSXPG	51
	iphone	C0036	Apple	iPhone Xr MT472LL/A	?

2.3. Collection of Flicker Data for Mixtures of Lights

To investigate the expression of flicker that might be present in VIIRS DNB data collected on pixels having large numbers of individual luminaires, high-speed camera data were collected for a set of scenes containing mixtures of light sources. We speculated that the magnitude of flicker would decline when large numbers of individual luminaires are viewed together. The first collection in the multi-light series was made on a wide range of luminaires from Table 1 placed together on an office table. This included LED streetlights, metal halides, high-pressure sodium, low-pressure sodium, incandescent, and fluorescent lights (Figure 5).

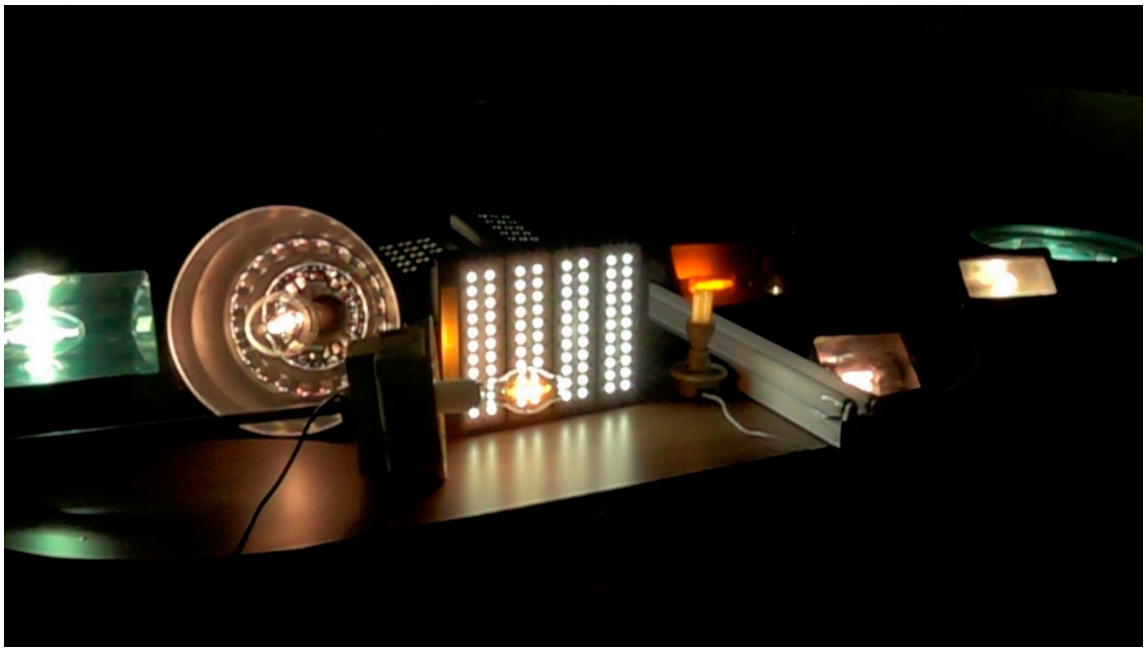

Figure 5. High-speed camera data were collected on a mixture of luminaires placed together on a table.

Next, we collected high-speed camera data (1000 frames per second) from the ground for three outdoor scenes containing large numbers of individual luminaires. This included: (1) Broomfield, Colorado's civic center (Figure 6), (2) the central zone of Golden, Colorado (Figure 7), collected from a viewpoint located on Lookout Mountain Road, and (3) Boulder, Colorado, viewed at a distance from a viewpoint along Highway 36 (Figure 8). The panoramic collections of Golden and Boulder cover large portions of each city as viewed from an oblique angle. The resulting temporal profiles from Golden and Boulder cover much larger areas than the individual DNB pixel footprint. The examination of the MP4 movies of these collections reveals the presence of a cacophony of sources ranging from lights having prominent flicker to lights having no visually evident flicker.

Figure 6. High-speed camera data were collected on a mixture of lights present at the Civic Center in Broomfield, Colorado. Also included in the scene was the moon—in the upper left-hand corner—which made it possible to analyze the flicker from the camera itself.

Figure 7. Oblique view of the mixture of lights presents in the central Golden, Colorado area collected with the high-speed camera. The data collection was from a viewpoint along Lookout Mountain Road west of Golden.

Figure 8. Panoramic view of Boulder, Colorado, from a viewpoint along Highway 36. High-speed camera data were collected covering the full sweep of lights visible in Boulder from the viewpoint.

To further investigate the remote sensing of flicker from the DNB, digital camera data were collected from a hovering drone carrying a slow-motion camera pointed in the nadir direction towards the earth. The experiment took place in the suburbs of Moscow, Russia (55.6321 north, 37.8622 east), at 01:00 local time on 29 November 2021. The vehicle was a DJI Air 2S drone with a built-in 4K video camera. The data were collected while the drone hovered 315 m above the earth's surface, resulting in a footprint of 600 × 600 m—slightly smaller than the DNB pixel footprint. The nighttime movie of the lights was recorded with FHD resolution 1920 × 1080, shutter speed 1/120 s, f/2.8 aperture, and sensitivity ISO 3200. The data were collected at 120 frames per second. The scene includes numerous flickering high-pressure sodium streetlights and parking lot lights, plus strings of white lights (Figure 9), with some clearly flickering and others with no obvious flickering.

Figure 9. View of lights collected at 120 frames per second from a hovering drone in Moscow, Russia.

2.4. Processing of the High-Speed Camera Data

The digital data from the high-speed camera MP4 movie frames were filtered to remove background pixels, which helped to concentrate the signal coming from the lights. The brightness of the remaining pixels in each frame were averaged and frame step times added. For the Sony camera, the frame steps were in millisecond increments since the camera ran at 1000 frames per second. The time step for the drone camera collection was 8.333 ms, corresponding to 120 frames per second. The result was a set of temporal profiles that were further analyzed to detect the presence and relative intensity of flicker.

An autocorrelation function (ACF) was used for the detection of flicker in the HSC data and a determination of the cycling rate in Hz. The ACF rates the similarity of the time series with itself for a series of evenly spaced temporal or lag increments [14]. For instance, if the data series is broken up into a series of consecutive five ms segments, the ACF calculates the degree of similarity found between the segments. This autocorrelation analysis is performed for all possible lag increments within the time series. The types of detectable temporal phenomena from the ACF analysis are dictated by the temporal increment of the data. For instance, annual cycling cannot be analyzed with annual nighttime lights data but can be analyzed with either nightly radiances [15] or average monthly radiances [16]. The presence of an AC flicker cycling in the high-speed camera data is indicated when an ACF peak exceeds the 95% or 99% confidence level threshold calculated via a z-statistic [17]. For an ACF sample size of 100 points, the 95% confidence threshold is 0.196, and the 99% confidence threshold is 0.258. A flicker rate of 120 Hz is indicated by the presence of a primary ACF peak at 8 ms, exceeding the 95% confidence thresholds (Figure 10).

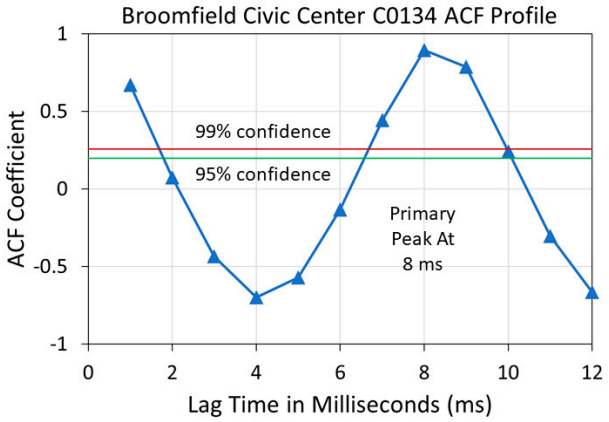

Figure 10. An autocorrelation function (ACF) is generated for each high-speed camera temporal profile to detect the presence of millisecond-scale cycling. The primary peak is defined as the highest local max lag value greater than 1 ms and exceeding 95% confidence. The Sony camera collected at 1000 frames per second. An ACF lag of 8 ms indicates the presence of 120 Hz flickering.

Calculations were made of the percent flicker and flicker index based on the methods described in the Lighting Handbook 10th Edition [18]; examples are shown in Figure 11. Note that in order to apply the flicker index to the randomized and actual DNB profiles, the definition had to be modified. In addition, the index of dispersion is calculated as the variance divided by the mean [19].

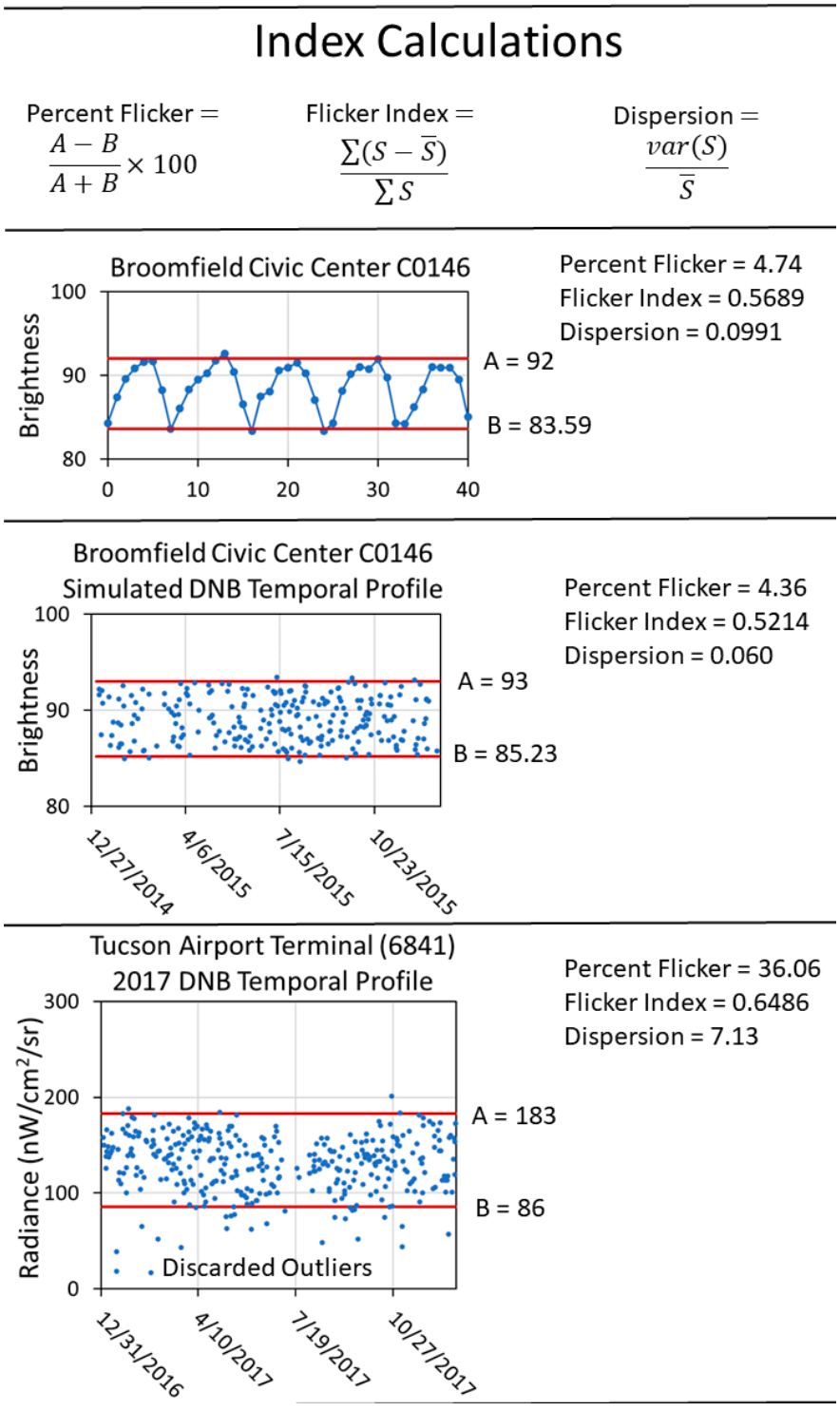

Figure 11. Calculation of percent flicker, flicker index, and index of dispersion.

Percent flicker is designed to quantify the amplitude of the flicker and is defined as:

$$\text{Percent Flicker} = \frac{\text{A} - \text{B}}{\text{A} + \text{B}} \times 100$$

For the high-speed camera temporal profiles, A is the average brightness of the upper peak, while B is the average brightness of the lower peak. For the simulated and actual DNB temporal profiles, A and B are the upper and lower limits of the core data range. Outlier removal and detrending may be required to obtain results that can be compared across samples.

The flicker index is designed to quantify the symmetry of the flicker and is defined as:

$$\text{Flicker Index} = \frac{\sum(S - \overline{S})}{\sum S}$$

where the S is the sample brightness, and $\overline{S}$ is the mean of sample brightness.

The dispersion index is defined as:

$$\text{Dispersion Index} = \frac{\text{var}(S)}{\overline{S}}$$

where $\text{var}(S)$ is the variance of sample brightness.

As with the percent flicker, outlier removal and trend removal may be advisable prior to the flicker index and dispersion calculations to yield consistent results.

2.5. Simulation of DNB Temporal Profiles from the High-Speed Camera Data

Because the VIIRS DNB temporal repeat cycle ranges from hours to days, the flicker patterns in lighting are sampled randomly. It is impossible to discern the lighting flicker rates with the ACF methodology using nightly time series of VIIRS DNB temporal profiles. However, we still want to test the flicker indices to evaluate their utility in analyzing the flicker effects present in DNB temporal profiles. Each DNB scanline has 4064 pixels and the HGS dwell time varies as a function of the sample position. The SNPP orbit processes, with a 16 day repeat cycle. That means the satellite repeats its orbital tracks every 16 days, with only minor deviations. The repeat cycle, combined with the spacecraft's precision orbit control, results in a series of narrowly defined "permissible" sample positions for any location on the ground. To mimic the variable temporal sampling of the HGS, we followed the sampling pattern established for a particular mid-latitude location, as shown in Figure 12. Any location would suffice due to the even mixture of sample positions over time. The Figure 12 template happens to be from Houston, Texas, and has 1946 cloud-free DNB pixels from 2012 to 2020, binned into 20 vertical sample position columns. In simulating the DNB temporal profile from each high-speed camera temporal profile, exactly 1946 samples are drawn randomly from the brightness profile using the sample positions from Figure 12. The randomly drawn sample positions point to the appropriate DNB temporal aggregation time via a look up table. The simulated DNB temporal profiles have the same brightness units and range as the original 1000 frame per second profiles but are randomized. The A and B inflection points used to calculate the percent flicker are taken to be the upper and lower brightness levels of the data cloud (Figure 11).

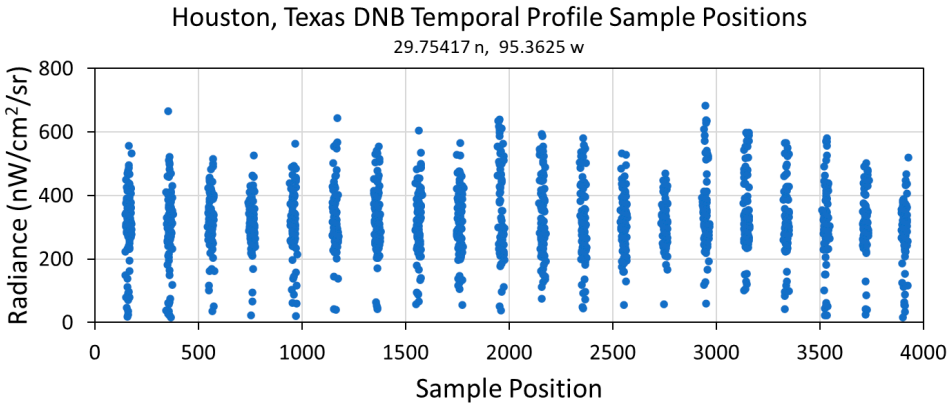

Figure 12. Sample position columns for the VIIRS DNB temporal profile from a 15-arcsecond grid cell in Houston, Texas. These columns define the sampling pattern for simulating the DNB temporal profiles from the high-speed camera data for each of the tested luminaires.

2.6. Examination of VIIRS DNB Temporal Profiles for Flicker Effects

To explore the detection of flicker in actual VIIRS data, a nightly DNB temporal profile grid was constructed for Tucson, Arizona. We generated the profiles at 15-arcsecond spacing, with 100 cells east–west and 72 cells north–south centered on Tucson (Figure 13). The DNB profiles were processed to remove sunlit and cloudy data. A satellite zenith angle normalization was applied to remove view angle effects [15]. A lunar illuminance adjustment was applied to subtract the reflected moonlight [15]. Cloudy pixels were filtered out based on the VIIRS cloud mask [16] generated by NOAA [20]. The annual mean, variance, and dispersion were then calculated for each 15-arcsecond grid cell.

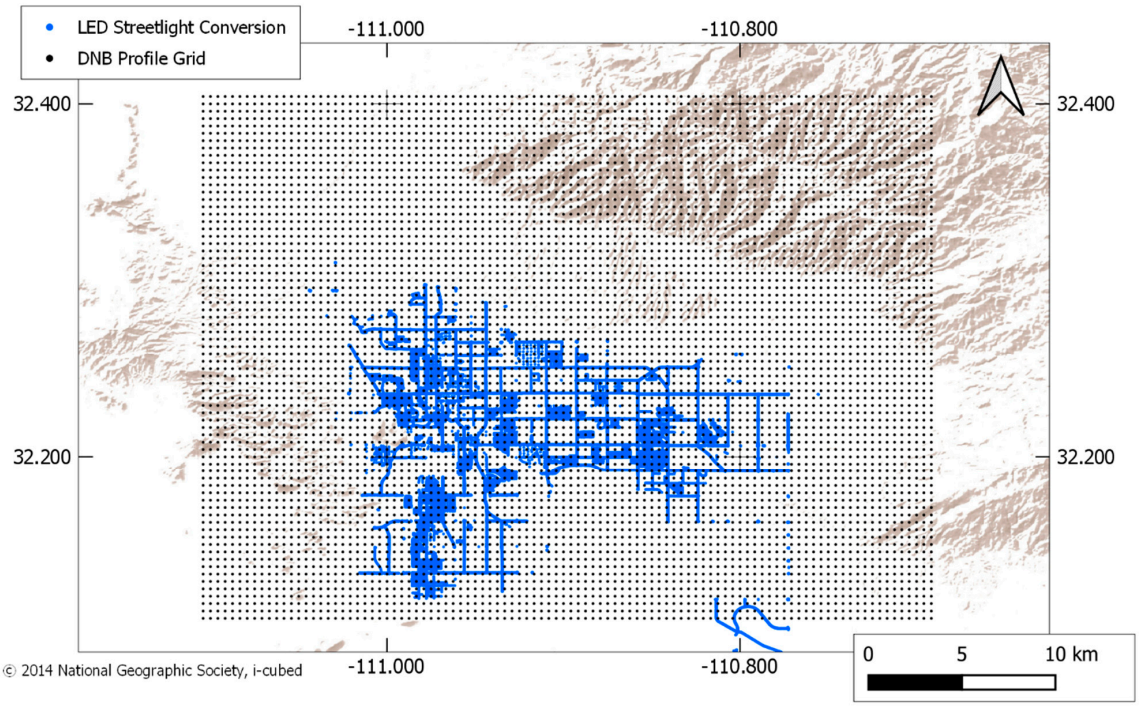

Figure 13. Outline of the VIIRS DNB temporal profile grid constructed for Tucson, Arizona. The locations of LED streetlight conversions are marked blue.

For decades, Tucson has taken actions to reduce light pollution to limit interference with several nearby astronomical observatories, such as Kitt Peak National Observatory. In 2016, the City of Tucson began replacing high-pressure sodium streetlights with LED

luminaires [21–23]. The motivation for the streetlight conversions was two-fold. There was a financial incentive, which was to reduce the power consumption and replacement cycle for individual luminaires. The other motivator was that the new system was designed to allow individual streetlights to be dimmed, thereby reducing light pollution. All of the city's nearly 20,000 streetlights were converted. It should be noted that other lighting present in the grid cells was unaffected by the city's LED conversion program. Following the conversion, the majority of the new LED streetlights have been operated at 60% capacity from midnight to dawn [21].

The grid cells are divided into three zones to examine the effects of the streetlight conversions on the index values. First, the grid cells are divided into those with and without detectable lighting (Figure 14). Background areas, devoid of detectable lighting, are defined based on annual average radiance values under one nanowatt/cm^2/sr. The lit grid cells are further divided into sets with and without City of Tucson LED streetlight conversions (Figure 15).

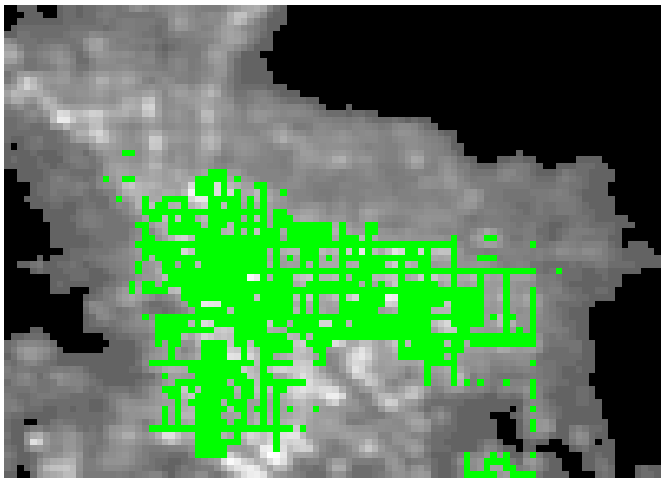

Figure 14. Average radiance image from Tucson for the combined years 2015 and 2017. Background areas, devoid of VIIRS detected lighting, are black. Grid cells with detectable lighting and no LED streetlight conversions are gray, and lit grid cells with LED streetlight conversions are green.

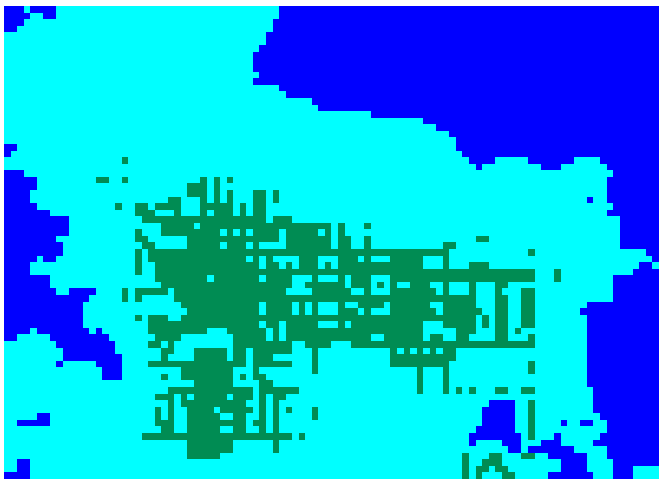

Figure 15. The DNB temporal profiles are divided into three categories: background (blue), lit and zero streetlight conversions (cyan), and lit with streetlight conversions (green). There are 1955 grid cells in the background, 4121 grid cells lit with no-LED conversions, and 1124 grid cells with LED streetlight conversions.

A set of five Tucson grid cells were selected for more detailed examination and testing. This included one grid cell from the background. The other four grid cells were selected because they show abrupt and dramatic changes in radiance levels, with two from the city's LED conversion zone and two from areas outside the city's LED conversion zone. For these five grid cells, the annual percent flicker, flicker index, and index of dispersion values were calculated.

3. Results

3.1. Re-Calculation of DNB Pixel Collection Times for HGS

The re-calculated SNPP DNB HGS pixel integration times are listed for each aggregation zone in Table 2 and shown graphically in Figure 16. The integration time is longest at nadir (2.68 ms) and shortest at the edge of scan (2.25 ms). The DNB pixel HGS-A and HGS-B integration times at nadir and edge of scan, shown overlaying a high-speed camera (1000 frames per second) temporal profile from a high-pressure sodium luminaire, are shown in Figure 17. The DNB HGS integration times are about one-third to one-fourth of the typical lighting flicker rates of 100 to 120 Hz.

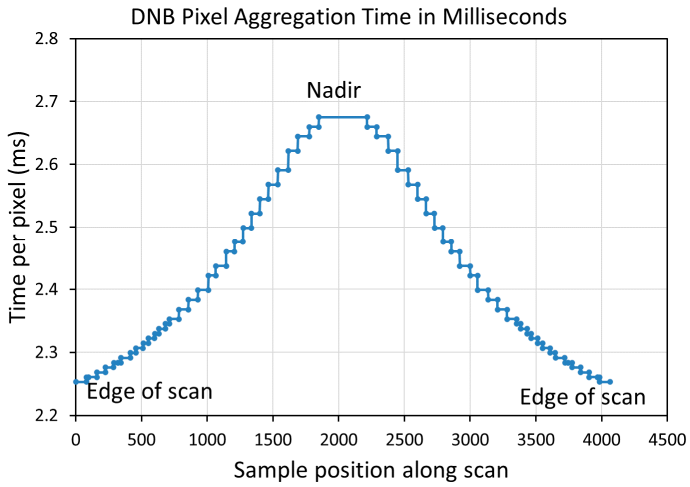

Figure 16. SNPP DNB pixel integration times by aggregation zone.

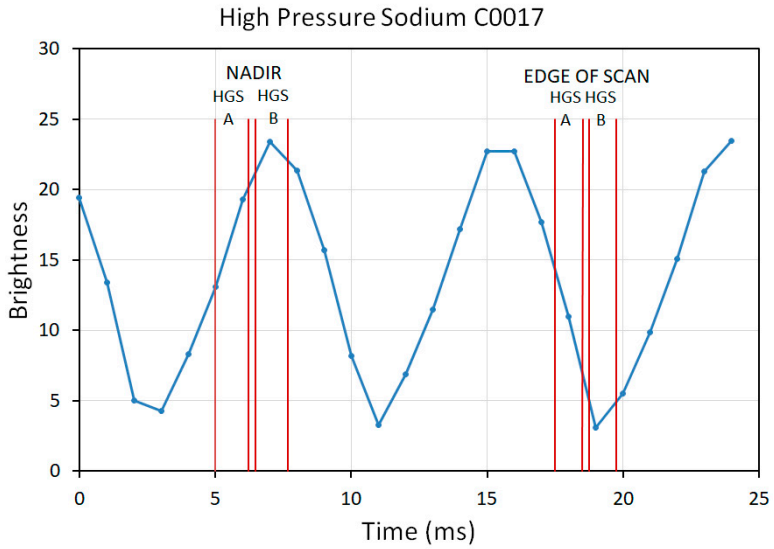

Figure 17. SNPP VIIRS DNB pixel integration times for HGS-A and HGS-B randomly placed over a high-pressure sodium temporal profile collected with the Sony high-speed camera. Each HGS sample consists of an A and a B side, separated by a 0.25 ms gap.

Table 2. SNPP VIIRS DNB pixel integration times by aggregation zone.

Aggregation Mode from Nadir	Number of Sub-pixels per Pixel		Number of Pixels per Mode	Time per Pixel (s) HGS-A	Time on HGS A-B Gap (s)	Time per Pixel (s) HGS-B	Total Time per DNB Pixel (s)
	Track Direction	Scan Direction					
1	42	66	184	1.21E-03	2.50E-04	1.21E-03	2.68E-03
2	42	64	72	1.20E-03	2.50E-04	1.20E-03	2.66E-03
3	41	62	88	1.20E-03	2.50E-04	1.20E-03	2.64E-03
4	40	59	72	1.19E-03	2.50E-04	1.19E-03	2.62E-03
5	39	55	80	1.17E-03	2.50E-04	1.17E-03	2.59E-03
6	38	52	72	1.16E-03	2.50E-04	1.16E-03	2.57E-03
7	37	49	64	1.15E-03	2.50E-04	1.15E-03	2.54E-03
8	36	46	64	1.14E-03	2.50E-04	1.14E-03	2.52E-03
9	35	43	64	1.12E-03	2.50E-04	1.12E-03	2.50E-03
10	34	40	64	1.11E-03	2.50E-04	1.11E-03	2.48E-03
11	33	38	64	1.11E-03	2.50E-04	1.11E-03	2.46E-03
12	32	35	80	1.09E-03	2.50E-04	1.09E-03	2.44E-03
13	31	33	56	1.09E-03	2.50E-04	1.09E-03	2.42E-03
14	30	30	80	1.07E-03	2.50E-04	1.07E-03	2.40E-03
15	29	28	72	1.07E-03	2.50E-04	1.07E-03	2.38E-03
16	28	26	72	1.06E-03	2.50E-04	1.06E-03	2.37E-03
17	27	24	72	1.05E-03	2.50E-04	1.05E-03	2.35E-03
18	27	23	32	1.05E-03	2.50E-04	1.05E-03	2.35E-03
19	26	22	48	1.04E-03	2.50E-04	1.04E-03	2.34E-03
20	26	21	32	1.04E-03	2.50E-04	1.04E-03	2.33E-03
21	25	20	48	1.04E-03	2.50E-04	1.04E-03	2.32E-03
22	25	19	40	1.03E-03	2.50E-04	1.03E-03	2.31E-03
23	24	18	56	1.03E-03	2.50E-04	1.03E-03	2.31E-03
24	24	17	40	1.02E-03	2.50E-04	1.02E-03	2.30E-03
25	23	16	72	1.02E-03	2.50E-04	1.02E-03	2.29E-03
26	23	15	24	1.02E-03	2.50E-04	1.02E-03	2.28E-03
27	22	15	32	1.02E-03	2.50E-04	1.02E-03	2.28E-03
28	22	14	64	1.01E-03	2.50E-04	1.01E-03	2.28E-03
29	21	13	64	1.01E-03	2.50E-04	1.01E-03	2.27E-03
30	21	12	64	1.01E-03	2.50E-04	1.01E-03	2.26E-03
31	20	12	16	1.01E-03	2.50E-04	1.01E-03	2.26E-03
32	20	11	80	1.00E-03	2.50E-04	1.00E-03	2.25E-03
Total			**2032**				7.71E-02

3.2. Results from High-Speed Camera Temporal Profiles for Individual Sources

Figure 18 shows representative examples of the high-speed camera temporal profiles from the 23 individual luminaires, including high-pressure sodium, metal halide, fluorescent, incandescent, and LED. The 120 Hz flicker pattern can be seen visually, though the clarity of the pattern is diminished in the LED streetlight.

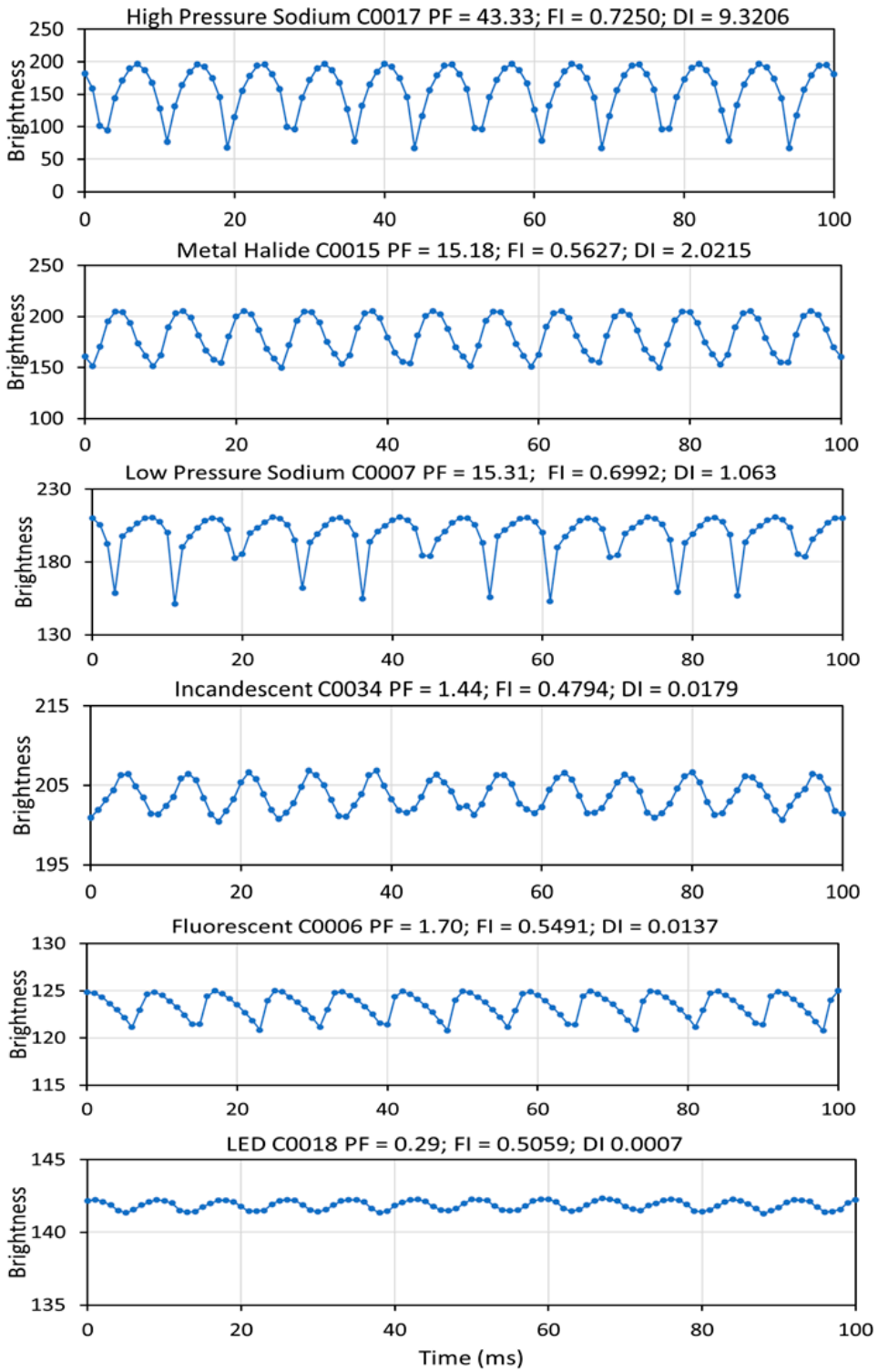

Figure 18. High-speed camera temporal profiles from a variety of individual luminaires. The brightness axis scaling has been adjusted to highlight the flicker pattern, which is weakest in the LED. The title line on each profile records the luminaire type, sample number, percent flicker (PF), flicker index (FI), and dispersion index (DI).

The temporal profiles were resampled to simulate DNB temporal profiles, a process that obliterates the cycling pattern evident in the millisecond temporal profiles (Figure 19). However, histograms from the DNB temporal profiles of individual luminaires continue to exhibit spikes near the low and high ends of brightness range, corresponding to the

flicker inflection points. The histogram spike pattern is characteristic of "harmonic oscillators" [24]. The histogram spikes occur due to the increased temporal dwell at nearly the same brightness level when the sample falls across either the upper or lower flicker inflection points.

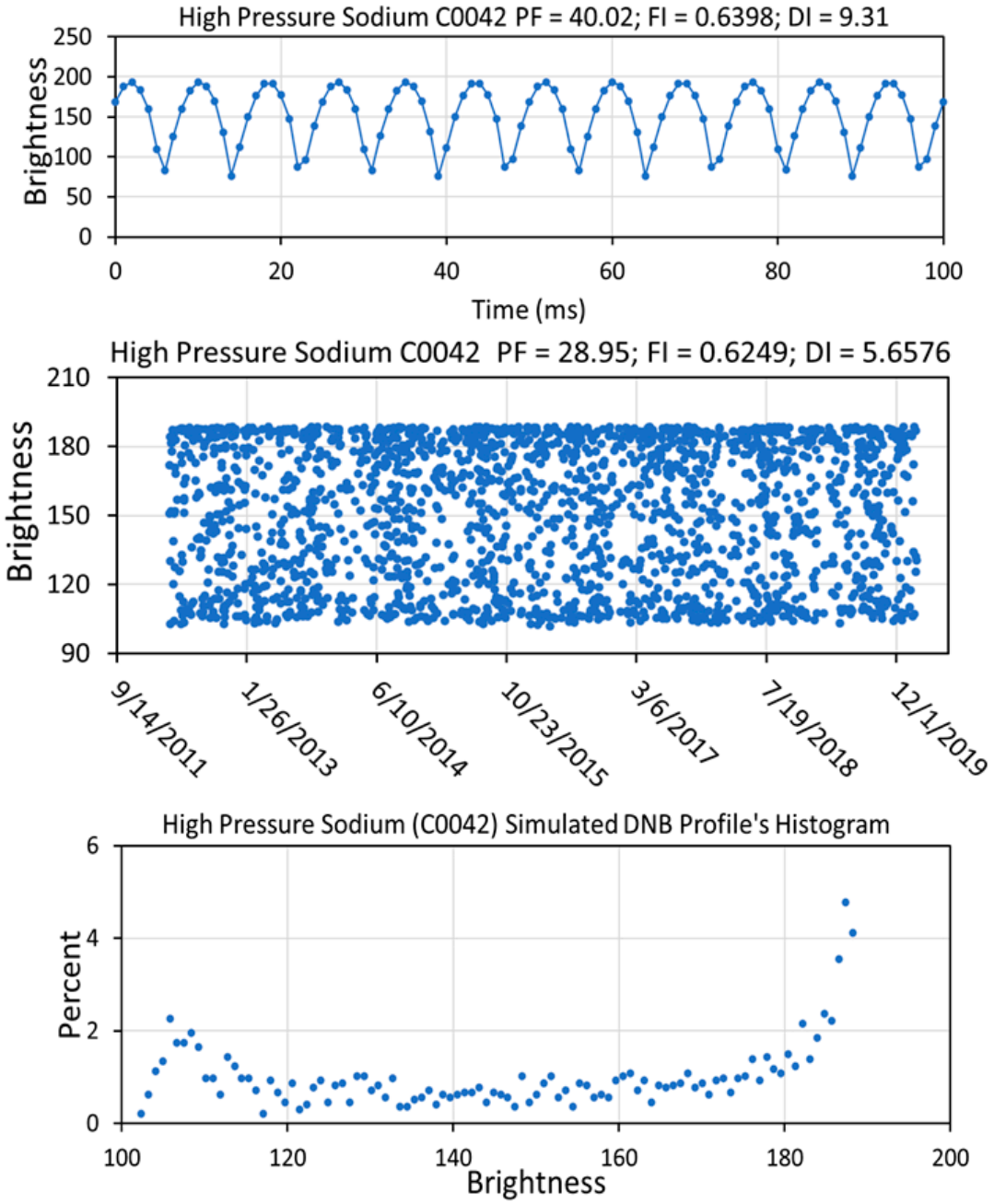

Figure 19. Simulated DNB temporal profile and associated histogram from the resampling of a metal halide high-speed camera temporal profile. Note that the brightness range of the simulated DNB temporal profile is slightly less than the original 1000 frames per second temporal profile, an expression of the temporal aggregation from the longer DNB pixel aggregation. The histogram shows spikes at brightness levels of 10.5 and 19, a vestigial expression of the flickering upper and lower sine wave peaks.

The flicker index and ACF results from the individual luminaires are summarized in Table 3. The table is sorted according to the percent flicker in descending order. The highest percent flicker values are found with the high-intensity discharge lamps, with the

two high-pressure sodium sources having the highest percent flicker, followed by the metal halides and low-pressure sodium. The LED streetlights and one of the fluorescent tubes have the lowest percent flicker.

Table 3. Flicker results for individual luminaires. SDNB = simulated DNB.

Luminaires	Number	% Flicker	Flicker Index	Dispersion	Flicker Hz	SDNB % Flicker	SDNB Flicker Index	SDNB Dispersion
Compact Fluorescent	C0028	68.12	0.8216	17.1248	120	38.59	0.7303	8.0688
High Pressure Sodium	C0017	43.33	0.7250	9.3200	120	28.69	0.6356	5.4270
High Pressure Sodium	C0042	40.02	0.6398	9.3078	120	28.95	0.6249	5.6576
Metal halide	C0012	21.71	0.5656	3.6492	120	18.49	0.5816	2.3106
Low Pressure Sodium	C0007	15.31	0.6992	1.0630	120	8.25	0.6051	0.4863
Metal Halide	C0015	15.18	0.5627	2.0215	120	12.40	0.5550	1.3042
Ceramic metal Halide	C0009	14.40	0.5754	1.7200	120	10.73	0.6237	1.0180
Metal Halide RAB	C0016	12.51	0.5956	1.7166	120	9.96	0.5474	0.8887
Incandescent	C0027	5.47	0.5108	0.2264	60	5.26	0.5464	0.2031
Fluorescent	C0006	1.70	0.5491	0.0137	120	1.23	0.5152	0.0080
Incandescent	C0034	1.44	0.4794	0.0179	120	1.23	0.5604	0.0128
Incandescent dual	C0033	1.30	0.4986	0.0135	120	1.14	0.5661	0.0093
Incandescent	C0014	1.06	0.5379	0.0118	120	1.16	0.5075	0.0077
iphone flashlight	C0036	0.77	0.4574	0.0047	0	0.53	0.6268	0.0016
Compact Fluorescent	C0031	0.65	0.5561	0.0031	120	0.47	0.6230	0.0018
Compact Fluorescent	C0032	0.63	0.3580	0.0028	120	0.59	0.5852	0.0013
LED	C0018	0.29	0.5059	0.0007	120	0.30	0.5049	0.0005
LED 4000 K	C0020	0.19	0.4897	0.0003	120	0.22	0.4930	0.0002
Compact Fluorescent	C0011	0.14	0.5450	0.0003	120	0.17	0.5378	0.0003
LED	C0026	0.12	0.5250	0.0002	120	0.12	0.5201	0.0001
LED 3000 K	C0022	0.10	0.4360	0.0001	120	0.11	0.5117	0.0001
Fluorescent Ceiling	C0035	0.08	0.5547	0.00004	120	0.09	0.6592	0.00004

Figure 20 shows representative examples of ACF profiles from the high-speed camera data and a grid cell in Tucson found to have weekly brightness cycling. The ACF analysis found 120 Hz flicker in 19 of 20 individual luminaires (Table 3). The ACF analysis found no detectable flicker from the iPhone flashlight (sample C0036).

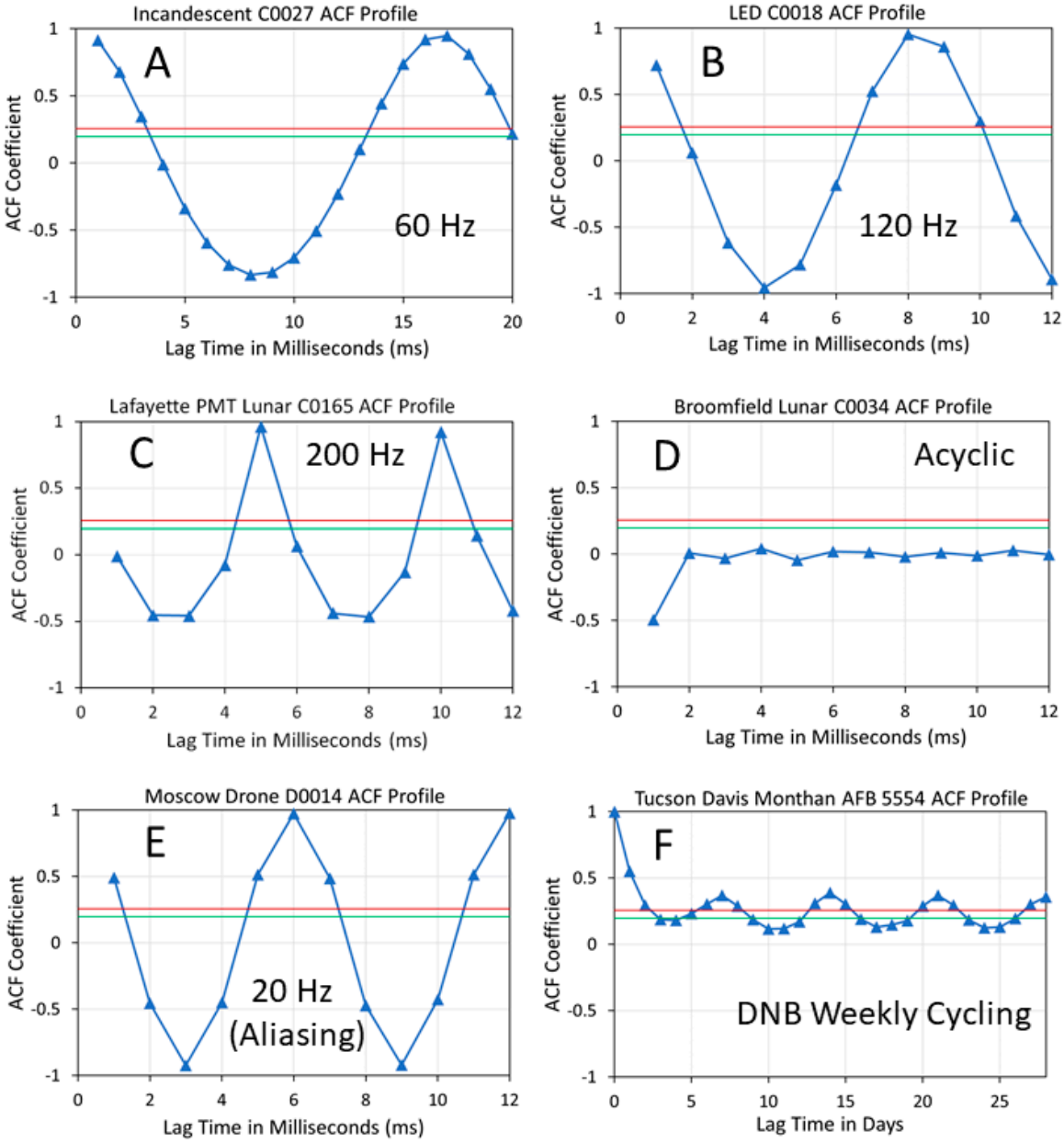

Figure 20. Examples of autocorrelation function (ACF) profiles from the study. (**A**) High-speed camera (HSC) data from a Sylvania incandescent light (C0027), (**B**) HSC data from an LED streetlight (C0018), (**C**) PMT-equipped HSC data from a lunar view, (**D**) HSC data from a lunar view, and (**E**) DJI Air 2S drone camera data of lights in Moscow, Russia, collected at 120 frames per second. The primary peak has a lag of six frames, indicating 20 Hz flickering. The actual flicker rate is 100 Hz. The discrepancy is due to aliasing. (**F**) VIIRS DNB nightly temporal profile of Davis Monthan Air Force Base, Tucson, Arizona. The seven-day lag indicates the presence of weekly cycling in the brightness of the lights.

Scattergrams were generated to examine the relationships between the three indices and the impact of DNB resampling. Figure 21 shows the percent flicker versus flicker index, with labeling of the lighting types. The luminaires with high percent flicker also have relatively high flicker index values, though it is not a well-defined linear relationship. In contrast, the index of dispersion is highly correlated to percent flicker (Figure 22).

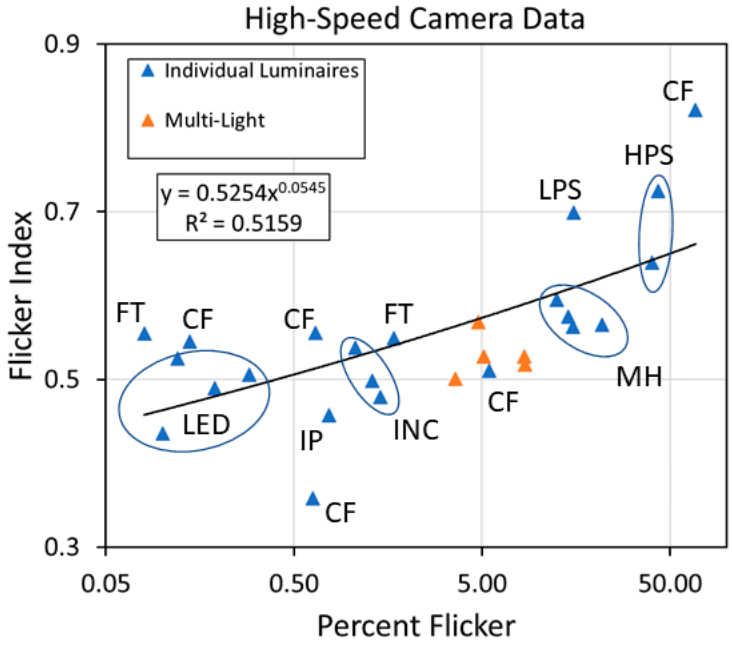

Figure 21. Percent flicker versus flicker index for individual luminaires, multi-light collections, and Tucson DNB profiles. The individual luminaires are clustered into types: HPS = high-pressure sodium, MH = metal halide, LPS = low-pressure sodium, INC = incandescent, CF = compact fluorescent, IP = iPhone flashlight, LED = LED streetlights, FT = fluorescent tubes.

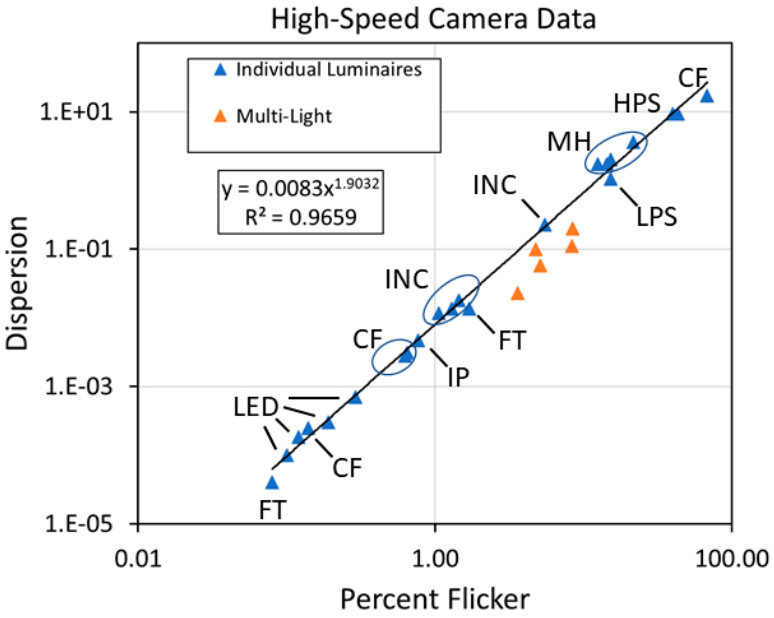

Figure 22. Percent flicker versus the index of dispersion for the HSC collections made of individual luminaires, multi-light collections, and DNB temporal profiles from Tucson.

The scattergram of percent flicker from the individual luminaires versus DNB simulated temporal profiles shows a highly linear relationship (Figure 23). There is a slight decline in the percent flicker values from the DNB-simulated temporal profiles, presumably due to the longer integration time of the DNB versus the Sony camera running at 1000 frames per second. The flicker index values from HSC temporal profiles versus their DNB-simulated equivalents are shown in Figure 24. Note that the DNB simulation results in compression in the flicker index range. Figure 25 shows that the index of dispersion values for HSC and DNB simulated temporal profiles are highly correlated.

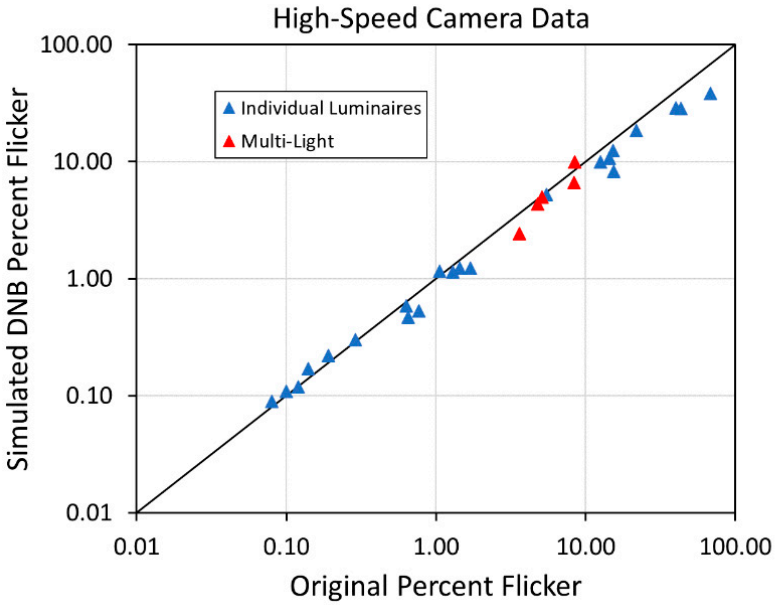

Figure 23. Percent flicker from the high-speed camera collections versus the DNB-simulated temporal profiles. The two are highly corelated, with the data cloud forming a diagonal. There is a slight loss in flicker index values for the DNB-simulated sets, presumably due to the longer integration time of the DNB compared to the digital camera data.

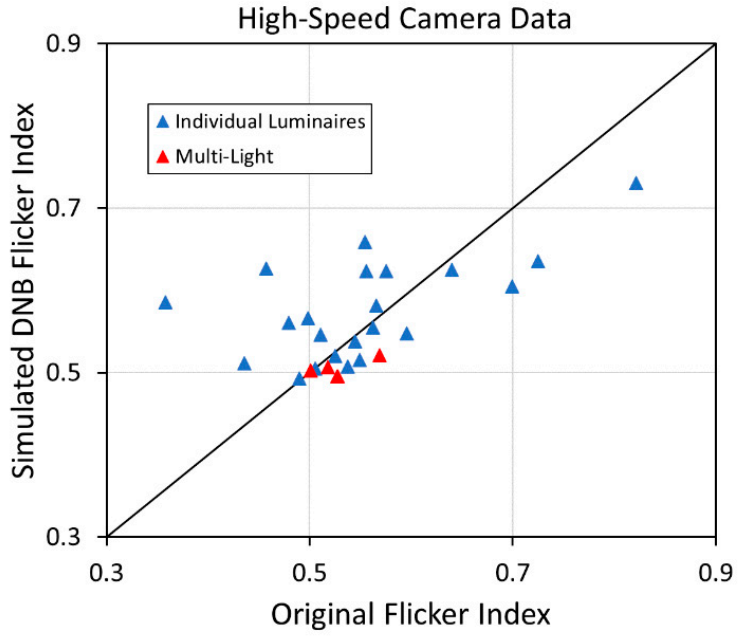

Figure 24. Flicker index values from the high-speed camera collections versus the DNB-simulated temporal profiles. The two data sets are not well correlated. Specifically, the flicker index data range from the simulated DNB temporal profiles is compressed, indicating a loss in the index's ability to distinguish different types of lighting.

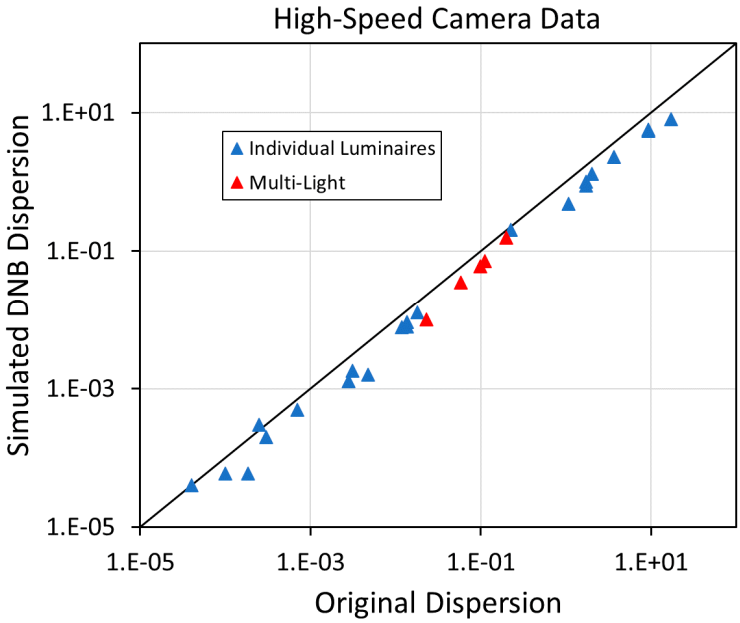

Figure 25. Index of dispersion values from the high-speed camera collections versus the DNB simulated temporal profiles. The two are highly corelated, with the data cloud forming a diagonal. The DNB-simulated profiles produced slightly lower dispersion values, presumably due to the longer integration time of the DNB compared to the digital camera data.

3.3. Results from Lunar Views

The lunar view temporal profiles from the Sony and PMT cameras are shown in Figure 26. These can be considered HSC collections of individual sources since all other sources are masked out. The temporal profiles from the Sony camera show a low level of background noise with no sign of flickering. The PMT's lunar profile shows prominent AC fluctuations. This led to the exclusion of the PMT collections from other parts of this study.

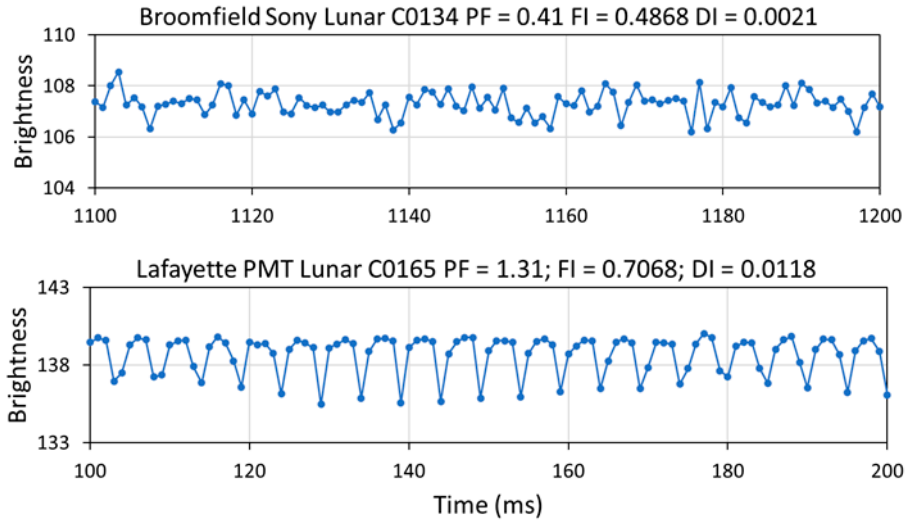

Figure 26. High-speed camera collections of the moon at night from the Sony camera (**top**) and the Sony camera equipped with a photo-multiplier tube (**bottom**). Note the prominent electronic flicker present in the PMT collection. This led to the exclusion of the PMT from further flicker study collections.

3.4. Results from High-Speed Camera Temporal Profiles for Multi-Light Collections

Figure 27 shows the high-speed camera temporal profiles from the multi-light collections from the table-top collection, oblique view of Golden, horizontal view of the Broomfield Civic Center, panoramic view of Boulder, and overhead view of outdoor lighting collected from a hovering drone in Moscow. Flicker is evident in each of the profiles, though it is more weakly expressed in the Golden and Boulder samples where the sample view covered lights present in multiple VIIRS DNB pixel footprints. The multi-light temporal profiles from Colorado feature 120 Hz flicker. Note that the horizontal axis scaling is expanded from 100 ms to 500 ms for the Moscow drone profile where the camera frame rate is 120 per second. The index results are reported in Table 4. All five of the multi-light temporal profiles had flicker present in the range of 3 to 5%. The ACF analysis found the flicker rate from Colorado to be 120 Hz, and the Moscow sample's to be 100 Hz.

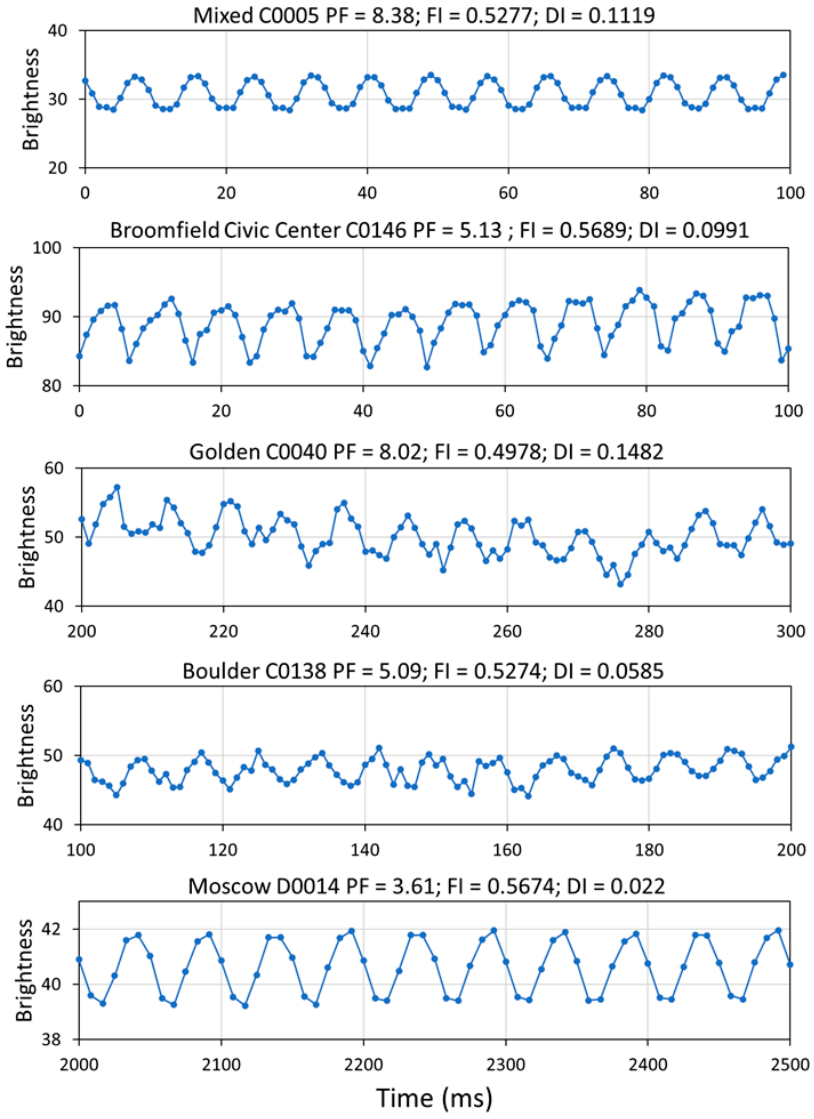

Figure 27. High-speed camera temporal profiles from five multi-light collections. Each of the samples shows visual evidence of AC flicker. The pattern is less clear in the Golden and Boulder examples, where the field-of-view covered multiple DNB pixels. Note that the temporal scale for the Colorado 1000 frames per second collection is standardized to 100 ms. The Moscow drone data were collected at 120 frames per second and a horizontal axis range of 500 ms to expose the flicker pattern. PF = percent flicker, FI = flicker index, DI = dispersion index.

Table 4. Multi-light camera collections. SDNB = simulated VIIRS DNB.

Observed Scene	Number	% Flicker	Flicker Index	Dispersion	Flicker Hz	DNB % Flicker	DNB Flicker Index	DNB Dispersion
Table Multilights	C0005	8.38	0.5277	0.1119	120	6.67	0.4953	0.072
Golden Panorama	C0040	8.43	0.5178	0.1972	120	9.92	0.5069	0.1581
Broomfield Civic Center	C0146	4.79	0.5689	0.0991	120	4.36	0.5214	0.06
Boulder Panorama	C0138	5.09	0.5274	0.0585	120	4.99	0.4956	0.0349
Moscow Drone	D0014	3.61	0.5008	0.0228	100	2.45	0.5026	0.0101

3.5. Examination of DNB Temporal Profiles of Tucson, Arizona

The VIIRS DNB profiles for five grid cells from the Tucson metropolitan area are shown in Figure 28. Percent flicker, flicker index, and index of dispersion calculations were made for each of the five temporal profiles to examine the value of the indices in detecting changes in flicker. For each site, one year is reported as a reference and a second year is reported as a subject. The results are shown in Table 5.

Table 5. Flicker index calculations for five Tucson grid cells.

Location	Cell Number	Reference Year	Ref. % Flicker	Ref. Flicker Index	Ref. Dispersion	2017 % Flicker	2017 Flicker Index	2017 Dispersion	LED Conversions
S. Kino Parkway and 22nd	4738	2015	21.21	0.5797	1.88	23.29	0.5148	0.91	61
Automall	2730	2015	63.77	0.677	13.92	59.09	0.6725	9.01	29
HomeGoods Distribution Center	6746	2014	99.99	0.6175	4.15	41.63	0.5644	10.87	0
Airport terminal	6841	2013	22.59	0.657	15.17	36.06	0.6457	7.13	0
Mt. Lemmon	100	2015	99.97	0.6426	0.422	99.96	0.6554	0.404	0

The South Kino Parkway grid cell covers a lit roadway and a commercial zone with streets and buildings. It had 61 LED streetlight conversions. The temporal profile started out in 2012 with a mean radiance of 46 nW and a variance of 141, more than three times the mean. There was an upward radiance trend from 2012 to 2015, leading to a 2015 mean of 62 nW and a variance of 117. In 2016, there was a rapid decline in both radiance and variance, likely in response to the reduction in streetlight voltages after midnight and the near absence of flicker in the LED streetlights. The radiant emission pattern remained stable from 2017 to 2021.

The Tucson Automall grid cell is centered on a large, brightly lit parking lot featuring a large number of metal halide and high-pressure sodium luminaires. Multiple car dealerships are located together and are reported to begin turning off portions of their lighting after the 8 p.m. showroom closures. The grid cell had 29 LED streetlight conversions. The temporal profile is distinctive relative to the others in Figure 28 for its high level of variance across all years, fluctuating from a high of 1796 in 2013 to a low of 568 in 2018. As with the Kino Parkway grid cell, there is a decline in the mean radiance in 2016 during the

LED conversion period. The mean radiance drops from 101 nW in 2015 to 72 nW in 2018. Following this, the mean radiance then slowly rebounds to 77 nW in 2021.

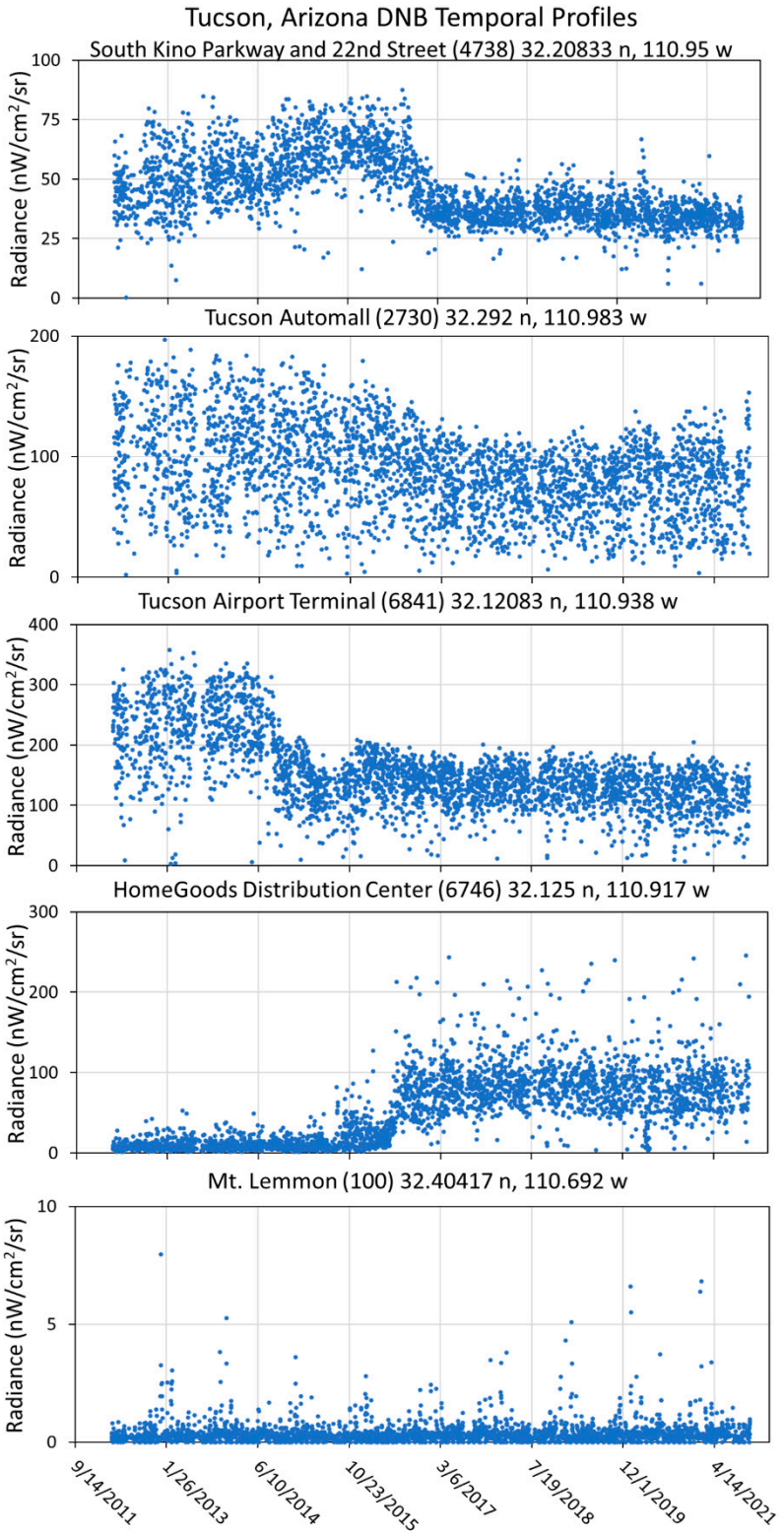

Figure 28. VIIRS DNB temporal profiles for five grid cells from Tucson, Arizona.

The Tucson International Airport (TUS) terminal grid cell contains the terminal building, parking lots, and a portion of the runway. It is one of the brightest locations found in Tucson, with zero LED streetlight conversions. The mean brightness started out with a

mean of 220 nW and variance of 3636 in 2012. The mean increased slightly until mid-2014, at which point there was a sharp dip in radiance which continued until mid-2015, a period of renovation with the conversion of many metal halide and high-pressure sodium outdoor lights to highly-shielded LEDs. Once the construction was complete, there was a slight radiance recovery in late 2015, and the emissions then stabilized to means near 120 nW and variances near 900 from 2017 to 2021.

The HomeGoods Distribution Center is an 850,000 square foot facility that held its grand opening on 14 October 2016 [25]. The DNB temporal profile shows a relatively modest and stable level of lighting present from 2012 to July 2015, with mean radiances near 10 nW and variances ranging from 35 to 50. The brightness dropped slightly in August of 2015 and then bumped up with the radiances frequently rising to the 20–30 nW range for the next year—the facilities construction phase. The brightness increased again at the end of June 2016, prior to the grand opening, and remained in a largely stable state, with mean radiances in the 80 to 90 nW range and variances in the 880 to 1000 range through 2021. There was a month-long radiance drop in April 2020, likely the result of a site-wide shut down during the COVID-19 pandemic.

The fifth individual grid cell being examined is representative of the unlit background, taken from the core of Mt. Lemmon, part of the Coronado National Forest. The DNB temporal profile features low mean radiances, in the range of 0.3 to 0.5 nW, indicating the absence of detectable lighting. Variances were also low, under 1 in each of the years. There was a series of radiance spikes, up to 8 nW on a winter night with high lunar illuminance, likely the result of moonlight reflecting off snow.

3.6. Examination of Annual Mean, Variance, and Dispersion across Tucson

The grid cells from the Tucson DNB temporal profile grid were divided into three zones: background (no lighting detected), lit and no-LED conversions, and lit with LED conversions. In this section, we examine the behavior of the lighting in the three zones prior to and following the completion of most of the LED conversions using the annual mean, variance, and index of dispersion from 2015 and 2017.

Figure 29 shows the scattergrams of the annual mean radiances for the three zones. There was a slight increase in the mean radiance for 71.6% of the grid cells in the background zone. The mean radiances were largely unchanged in the lit grid cells with no LED streetlight conversions. In contrast, the mean radiance declined for 97% of the grid cells with LED conversion from 2015 to 2017.

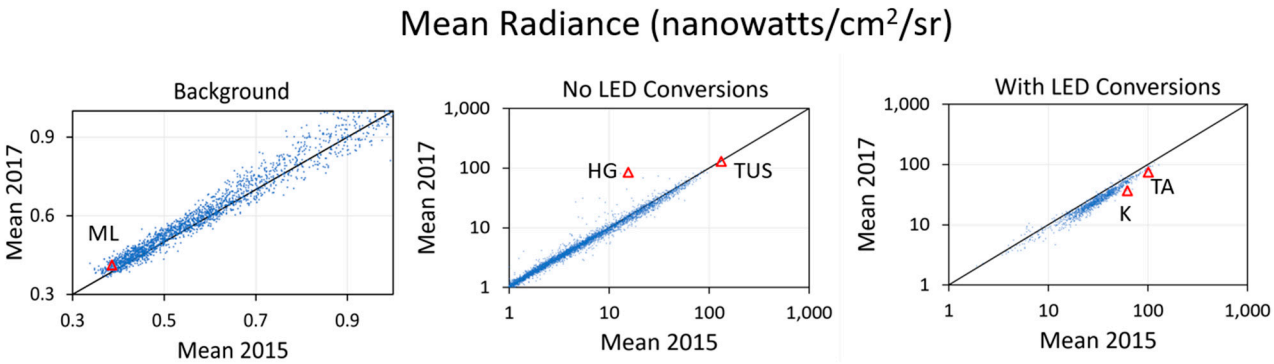

Figure 29. Mean radiance scattergrams for the three zones for 2015 versus 2017. The diagonal lines indicate equal values in the two years. There was a minor increase in the mean radiance in 2017 for the background grid cells. The mean radiance stayed nearly constant for lit grid cells lacking LED streetlight conversions, tracking the diagonal. Mean radiance declined in 97% of the grid cells with LED streetlight conversions. Red triangles correspond to the five Tucson DNB profiles shown in Figure 28: ML = Mount Lemmon; HG = HomeGoods Distribution Center; TUS = Tuscon International Airport; K = South Kino Parkway; TA = Tucson Automall.

Figure 30 shows the scattergrams of the annual variance for the three zones for 2015 versus 2017. The grid cells in the background zone changed very little in variance from 2015 to 2017, with the data cluster centered on the diagonal. There was a discernable decline in variance for a small portion of the background grid cells. For the lit zone with no-LED conversions, 74.6% of the lit grid cells had a decline in variance. Amongst the grid cells with LED streetlight conversions, 92.6% had a decline in variance in 2017 relative to 2015.

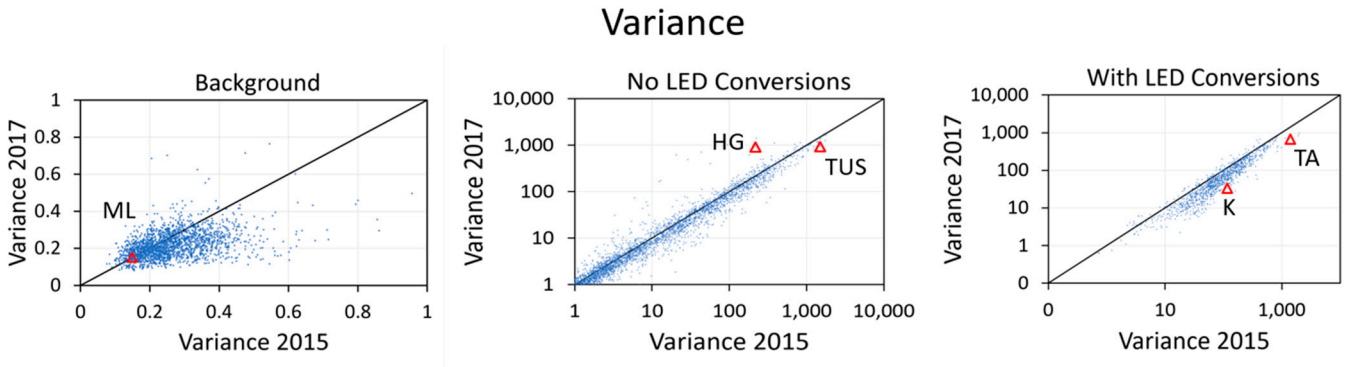

Figure 30. Variance scattergrams from the three zones for 2015 versus 2017. The diagonal lines indicate equal values in the two years. The grid cells in the background zone were largely stable in variance, with only a small portion of the grid cells dropping slightly in variance in 2017 relative to 2015. For the lit grid cells with no LED streetlight conversion, 74.6% had a slight decline in variance in 2017. In contrast, 92.6% of the grid cells with LED streetlight conversions had a decline in variance in 2017. Red triangles correspond to the five Tucson DNB profiles shown in Figure 28: ML = Mount Lemmon; HG = HomeGoods Distribution Center; TUS = Tuscon International Airport; K = South Kino Parkway; TA = Tucson Automall.

Figure 31 shows the scattergrams of the annual index of dispersion for the three zones for 2015 versus 2017. There was a slight decrease in the dispersion for the background zone. The dispersion is largely unchanged in the lit zone with no LED streetlight conversions. There is a decline in the dispersion in 2017 compared to 2015 for 79.3% of the grid cells with LED streetlight conversions.

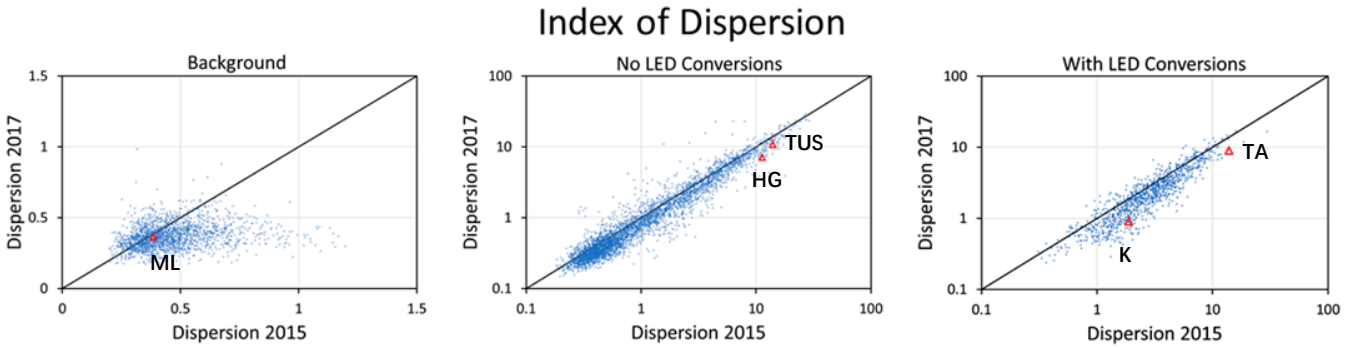

Figure 31. Index of dispersion scattergrams for the three zones for 2015 versus 2017. The diagonal lines indicate equal values in the two years. The grid cells in the background zone were largely stable in dispersion, with only a small portion of the grid cells dropping slightly in variance in 2017 relative to 2015. For the lit grid cells with no LED streetlight conversion, 74.8% had a decline in dispersion in 2017. In contrast, 79.3% of the grid cells with LED streetlight conversions had a decline in dispersion in 2017. Red triangles correspond to the five Tucson DNB profiles shown in Figure 28: ML = Mount Lemmon; HG = HomeGoods Distribution Center; TUS = Tuscon International Airport; K = South Kino Parkway; TA = Tucson Automall.

4. Discussion

The recalculation of the VIIRS DNB HGS pixel aggregation time finds that the pixel collection times vary from 2.25 to 2.68 ms. This is substantially shorter than the 8.3 ms cycle for the lighting flicker associated with a 60 Hz alternating current. Of the lighting types measured, flicker is most prominent in high-intensity discharge (HID) luminaires such as high-pressure sodium and metal halide, which are widely used in outdoor lighting. Compared to HID sources, flicker is reduced in incandescent and fluorescent lights. Fluorescent light fixtures frequently include capacitors, which reduce the voltage fluctuations that cause flicker. The thermal inertia of incandescent filaments serves as an inbuilt capacitor, reducing flicker to a greater degree than HID sources. Over the years, LED manufacturers have invested in the development of "constant-current" drivers [26] that have largely eliminated flicker in today's LED streetlights.

Evidence for the effects of flicker can be seen in VIIRS DNB temporal profiles from Tucson sites where LED conversion projects replaced HID streetlights with low-flicker LED sources. Both the South Kino Parkway and Tucson Airport temporal profiles start out with high radiance levels and high variance. The conversion period is indicated by noticeable drops in radiance levels. Upon completion of the LED conversions, the radiance levels stabilize at a reduced level and both variance and dispersion are reduced. The radiance drop is likely the result of voltage reductions after midnight, plus the improved shielding of the new LED streetlights. In the grid cells where the variance reductions exceed that radiance reduction, there is a decline in dispersion. This occurred in 79.3% of the Tucson grid cells with LED streetlight conversions. This decline in the dispersion indicates that the flicker was reduced when the high-flicker HID lights were replaced with low-flicker LED lights.

Three indices were tested for their ability to detect changes in the flicker levels in VIIRS DNB temporal profiles, including percent flicker, flicker index, and the index of dispersion. Percent flicker and the flicker index are standard measurements developed to detect and quantify flicker by the lighting engineering community. All three indices performed well for the individual luminaires listed in Table 3. For the VIIRS DNB profiles, the index testing contrasted the values from a reference year and a subject year, selected to straddle an obvious change in the lighting behavior. The DNB profile index results (Table 4) indicate that the percent flicker and flicker index did not perform as well as the index of dispersion. The grid cell from Figure 16 with the highest percent flicker is from Mt. Lemmon—a background area devoid of lighting. The percent flicker remained nearly constant for the South Kino Parkway grid cell, which had 61 LED streetlight conversions, resulting in a substantial reduction in variance. Similar issues were found for the flicker index, which jumped by two orders of magnitude for the Mt. Lemmon grid cell and remained largely unchanged for the South Kino Parkway and Tucson Airport grid cells, which had large numbers of HID-to-LED conversions. Our assessment is that the index of dispersion is better than the percent flicker and flicker index for the detection and analysis of flicker in VIIRS DNB temporal profiles.

5. Conclusions

Back to the original question, is the VIIRS DNB a flicker meter in space? The answer is "yes" and "no". The DNB HGS pixel integration time is more than three times shorter than the 100 to 120 Hz flicker found in lighting. However, VIIRS is incapable of measuring the flicker rates in Hz due to the fact that the DNB's repeat cycle is measured in hours rather than milliseconds. The VIIRS DNB differs from conventional flicker meters in that it is unable to collect coherent flicker cycles from spaces. Instead, the DNB integrates radiances from all of the surface lighting present in pixel footprints and collects for 2–3 ms nightly with hour- to day-long gaps between observations. This implies that if flicker is present at the pixel footprint level, the recorded VIIRS radiance will fluctuate unpredictably over time, making it a source of instantaneous dispersion. This instability is expressed as an enhanced level of variance in long-term DNB temporal profiles. Because the VIIRS pixel footprints are

about half a square kilometer, there can be many individual lights present and contributing to the radiance observed by the DNB. If the flickering lights are not synchronized, the observable radiance pattern is an erratic cacophony, with multiple offset flicker patterns tending to cancel each other out. An AC flicker pattern can emerge from the cacophony, though it will be a weak signal compared to that found in individual sources.

Several recent studies [15,27] have enumerated the factors that introduce variance into VIIRS DNB temporal profiles, such as the view angle, atmospheric variability, cloud-effects, cycling of lunar illuminance, snow cover, and even deciduous tree phenology. To this, we should add flicker and the variability of flicker within DNB pixel footprints that are assembled in the construction of DNB temporal profiles. The distinction between flicker and these other variables is that flicker is an instantaneous source of dispersion, and the other sources operate with longer time constants. Together, these variables produce a cloud of radiance dispersion in long-term DNB temporal profiles. The stability of DNB temporal profiles can be improved by adjusting the radiance levels for individual pixels designed to remove these influences. The purpose of cloud-screening is to reduce the radiance dispersion induced by cloud obscuration, a variability that is unrelated to actual surface lighting. Satellite zenith angle effects can be analyzed and removed via normalization [15]. It is also possible to isolate and remove fluctuations associated with lunar, weekly and annual cycling from DNB temporal profiles. However, no amount of adjustment for the environmental and geometric effects on DNB radiances can remove the effects of lighting flicker. Thus, flicker, if present at the pixel level, imprints itself indelibly on the DNB temporal profiles and sets an implicit limitation on the uncertainty of applications that utilize the DNB observations of artificial lights.

It is possible to collect data on flicker levels with high-speed cameras. A frame rate of 1000 per second makes it possible to observe flicker patterns in good detail. It appears feasible to collect quantitative flicker information for footprints approximating the DNB with high-speed cameras from hovering drones. One caution is that it is important to test the camera for the presence of electronic flicker by viewing the moon or daylit surface devoid of AC flicker.

The data from a high-speed camera collected on a wide range of luminaires indicate that high-intensity discharge (HID) luminaries, such as high- and low-pressure sodium and metal halides, are particularly prone to high levels of flicker. In contrast, modern LED luminaires are virtually devoid of flicker. This fact should be considered when designing ground-based DNB calibration sources. LED sources are vastly better than HID sources for DNB calibration sources. This fact casts doubt on the value of DNB calibration efforts where HID sources are utilized [28,29].

We examined the DNB temporal profiles from grid cells known to have had HID-to-LED conversions in Tucson, Arizona. The DNB profiles reveal the conversion date range, and the reduction in flicker effects that occurs when temporally unstable HID luminaires are replaced with steady LED sources. Three annual indices were tested for detecting and characterizing flicker in DNB temporal profiles, including percent flicker, flicker index, and the index of dispersion. The preliminary results indicate that the index of dispersion is the best of the three. The flicker index values calculated from the DNB temporal profiles have a compressed range and show little change between the pre- and post-LED streetlight conversion radiance profiles. Percent flicker operates suitably in lit grid cells but produces anomalously high values for background grid cells.

It should be noted that the flicker effects on VIIRS DNB data cannot be detected or analyzed using the current VIIRS monthly or annual nighttime light products, which only report the average cloud-free radiance [30,31]. The analyses from Tucson were based on nightly DNB temporal profiles. Our results indicate that the information value of monthly and annual VIIRS DNB products can be improved by producing the full suite of statistical moments (mean, variance, skew, and kurtosis). The mean and variance can be further processed to calculate the index of dispersion.

Over time, outdoor lighting flicker is being reduced as high-pressure sodium and metal halide sources are replaced with constant-current LED streetlights [32]. The results from Tucson indicate that the loss of flicker and dimming of the upwelling radiances associated with LED conversions can be detected and quantified with VIIRS DNB temporal profiles. While the transition to LED is primarily based on economics, there may be human health impacts. Several studies have noted the adverse health impacts of white LEDs, where the blue component is enhanced [33,34]. In contrast, the reduction in flicker associated with LED conversions may have beneficial effects on humans, a possibility that should be further investigated.

Our results shed some light on the sensor requirements for the observation of flicker rates and amplitudes. Flicker can be detected and analyzed with high-speed camera data. Such data can be collected on the ground or from the air. The collection platform should be stabilized with a tripod on the ground or by hovering in the air. Airborne surveys of flicker will be the easiest way to investigate the spatial patterns of flicker synchronization associated with multiple lights operating from a common AC power supply. It may be possible to map boundaries between power grid entities based on the discontinuities in flickering. From satellites, it may be possible to observe the flicker rates and amplitudes with high-speed, low-detection-limit cameras capable of staring at lights present on the earth's surface. This could be done from geostationary orbit or with pointable sensors in lower orbit.

In conclusion, VIIRS DNB-measured radiances from artificial light sources are affected by several phenomena, including flicker. The flicker effects can be concentrated by filtering out the pixels contaminated by cloud cover and adjusting the DNB radiances for effects such as lunar reflectance, view angle, and atmospheric variability. In addition, outlier and trend removal may be required to achieve consistent results. After the extraneous effects are removed or compensated for, DNB temporal profiles can reveal details of lighting development and conversions from high-flicker to low-flicker sources.

Author Contributions: Conceptualization, data collection, analysis, figure preparation, and writing: C.D.E.; data collection and analysis: M.Z.; data collection and provision of luminaires: D.K.; data collection, manuscript review, and editing: S.D.M., S.J.A., P.C.S. and D.H.; data collection and DNB temporal profile generation: F.C.H.; details on Tucson study sites: J.B., C.K.M. and C.C.M.K.; conceptualization and administrative support: M.B.; conceptualization: J.T.; manuscript review and editing: J.B., W.S.K., D.W.P., C.C.M.K., T.G. and D.H. All authors have read and agreed to the published version of the manuscript.

Funding: This research was funded by the Rockefeller Foundation, grant number 2018 POW 004 (Prof. Jay Taneja, principal investigator) and the NOAA Joint Polar Satellite System (JPSS) proving ground program project on VIIRS detection of COVID impacts on lighting (Prof. Steve Miller, principal investigator). Dr. Kyba is funded by Helmholtz Association Initiative and Networking Fund (CS-003).

Data Availability Statement: The VIIRS DNB temporal profile grid of Tucson is available at: https://eogdata.mines.edu/wwwdata/hidden/dnb_profiles_deliver_licorr/usa_tucson2/ (accessed on 6 March 2022).

Acknowledgments: The VIIRS data used in the research are the result of many years of development and satellite operations sponsored jointly by NASA and NOAA. Funding for the study came from NOAA's Joint Polar Satellite System (JPSS) proving ground study on COVID effects on lighting (Steven Miller, principal investigator) and the Rockefeller Foundation's e-guide project, grant 2018 POW 004 (Jay Taneja, principal investigator). Jeff Puschell of Raytheon Corporation assisted in clarifying the DNB pixel aggregation timeline. We are thankful to Eng. Artem Khuramshin (Hewlett Packard, Russia) for providing and operation of the drone during the slow-motion filming of streetlights in Moscow.

Conflicts of Interest: The authors declare no conflict of interest.

References

1. Mirra, C. *Flicker Measurement and Evaluation*; Union Internationale d'Electrothermie, Group de Travail Perturbations: Paris, France, 1986.
2. Fan, Y.H.; Wu, C.J.; Fan, C.C.; Chih, K.W.; Liao, L.D. A Novel Time Based Current Compensator for LED Back Light Modules. *Key Eng. Mater.* **2007**, *364–366*, 377–382. [CrossRef]
3. Bartley, S.H. The neural determination of critical flicker frequency. *J. Exp. Psychol.* **1937**, *21*, 678. [CrossRef]
4. Wilkins, A.; Veitch, J.; Lehman, B. LED lighting flicker and potential health concerns: IEEE standard PAR1789 update. In Proceedings of the 2010 IEEE Energy Conversion Congress and Exposition, ECCE, Atlanta, GA, USA, 12–16 September 2010; pp. 171–178. [CrossRef]
5. Wilkins, A.J. Health and efficiency in lighting practice. *Energy* **1993**, *18*, 123–129. [CrossRef]
6. Price, L.L.A. Can the Adverse Health Effects of Flicker from LEDs and Other Artificial Lighting Be Prevented? *LEUKOS* **2017**, *13*, 191–200. [CrossRef]
7. Davis, J.; Hsieh, Y.-H.; Lee, H.-C. Humans perceive flicker artifacts at 500 Hz. *Sci. Rep.* **2015**, *5*, 7861. [CrossRef]
8. IEEE Recommended Practices for Modulating Current in High-Brightness LEDs for Mitigating Health Risks to Viewers. IEEE-SA Standards Board, 26 March 2015. Available online: http://www.bio-licht.org/02_resources/info_ieee_2015_standards-1789.pdf (accessed on 5 March 2022).
9. Takahashi, T.; Tsukahara, Y.; Nomura, M.; Matsuko, H. Pokemon Seizures. *Neurol. J. Southeast Asia* **1999**, *4*, 1–11. Available online: http://www.neurology-asia.org/articles/19991_001.pdf (accessed on 5 March 2022).
10. Inger, R.; Bennie, J.; Davies, T.W.; Gaston, K.J. Potential biological and ecological effects of flickering artificial light. *PLoS ONE* **2014**, *9*, e98631. [CrossRef]
11. Schakel, M.; Banerjee, K.; Bergen, T.; Blattner, P.; Bouroussis, C.; Dekker, P.; Klej, A.; Li, C.; Ootake, H.; Reiners, T.; et al. *Guidance on the Measurement of Temporal Light Modulation of Light Sources and Lighting Systems*; Technical Note 12; International Commission on Illumination: Vienna, Austria, 2021. [CrossRef]
12. Baker, N.; Joint Polar Satellite System (JPSS); Visible Infrared Imaging Radiometer Suite (VIIRS); Sensor Data Records (SDR); Algorithm Theoretical Basis Document (ATBD). Goddard Space Flight Centre, Greenbelt Maryland, Ground Project Code, 474,474-00053. 22 April 2011. Available online: https://www.star.nesdis.noaa.gov/jpss/documents/ATBD/D0001-M01-S01-004_JPSS_ATBD_VIIRS-Geolocation_A.pdf (accessed on 7 March 2022).
13. Elvidge, C.D.; Keith, D.M.; Tuttle, B.T.; Baugh, K.E. Spectral identification of lighting type and character. *Sensors* **2010**, *10*, 3961–3988. [CrossRef]
14. Box, G.E.P.; Jenkins, G.M.; Reinsel, G.C. Autocorrelation Function and Spectrum of Stationary Processes. In *Time Series Analysis*; Wiley Online Library: Hoboken, NJ, USA, 2008; ISBN 9781118619193.
15. Elvidge, C.D.; Hsu, F.-C.; Zhizhin, M.; Ghosh, T.; Taneja, J.; Bazilian, M. Indicators of electric power instability from satellite observed nighttime lights. *Remote Sens.* **2020**, *12*, 3194. [CrossRef]
16. Hsu, F.; Zhizhin, M.; Ghosh, T.; Elvidge, C.; Taneja, J. The Annual Cycling of Nighttime Lights in India. *Remote Sens.* **2021**, *13*, 1199. [CrossRef]
17. Ord, J.K.; Getis, A. Testing for local spatial autocorrelation in the presence of global autocorrelation. *J. Reg. Sci.* **2001**, *41*, 411–432. [CrossRef]
18. The Illuminating Engineering Society of North America. *The Lighting Handbook: Reference and Application*, 10th ed.; IESNA: New York, NY, USA, 2011; 1328p.
19. Selby, B. The index of dispersion as a test statistic. *Biometrika* **1965**, *52*, 627–629. [CrossRef]
20. Kopp, T.J.; Thomas, W.; Heidinger, A.K.; Botambekov, D.; Frey, R.A.; Hutchison, K.D.; Iisager, B.D.; Brueske, K.; Reed, B. The VIIRS Cloud Mask: Progress in the First Year of S-NPP toward a Common Cloud Detection Scheme. *J. Geophys. Res. Atmos.* **2014**, *119*, 2441–2456. [CrossRef]
21. Barentine, J.C.; Walker, C.E.; Kocifaj, M.; Kundracik, F.; Juan, A.; Kanemoto, J.; Monrad, C.K. Skyglow changes over Tucson, Arizona, resulting from a municipal LED street lighting conversion. *J. Quant. Spectrosc. Radiat. Transf.* **2018**, *212*, 10–23. [CrossRef]
22. Barentine, J.C.; Kundracik, F.; Kocifaj, M.; Sanders, J.C.; Esquerdo, G.A.; Dalton, A.M.; Foott, B.; Grauer, A.; Tucker, S.; Kyba, C.C.M. Recovering the city street lighting fraction from skyglow measurements in a large-scale municipal dimming experiment. *J. Quant. Spectrosc. Radiat. Transf.* **2020**, *253*, 107120. [CrossRef]
23. Kyba, C.C.M.; Ruby, A.; Kuechly, H.U.; Kinzey, B.; Miller, N.; Sanders, J.; Barentine, J.; Kleinodt, R.; Espey, B. Direct measurement of the contribution of street lighting to satellite observations of nighttime light emissions from urban areas. *Light. Res. Technol.* **2021**, *53*, 189–211. [CrossRef]
24. Dick, R. Chapter 6—Harmonic Oscillators and Coherent States. In *Advanced Quantum Mechanics*; Springer: Berlin/Heidelberg, Germany, 2012.
25. City of Tucson. HomeGoods Distribution Center Holds Grand Opening. 16 October 2016. Available online: https://www.tucsonaz.gov/ward-5/news/homegoods-distribution-center-holds-grand-opening (accessed on 28 November 2021).
26. Dazhong, S.H.Z. Constant Current Driver for Semiconductor Lighting. *Res. Prog. SSE Solid State Electron.* **2006**, *2*.
27. Wang, Z.; Román, M.O.; Kalb, V.L.; Miller, S.D.; Zhang, J.; Shrestha, R.M. Quantifying uncertainties in nighttime light retrievals from Suomi-NPP and NOAA-20 VIIRS Day/Night Band data. *Remote Sens. Environ.* **2021**, *263*, 112557. [CrossRef]

28. Ryan, R.E.; Pagnutti, M.; Burch, K.; Leigh, L.; Ruggles, T.; Cao, C.; Aaron, D.; Blonski, S.; Helder, D. The Terra Vega active light source: A first step in a new approach to perform nighttime absolute radiometric calibrations and early results calibrating the VIIRS DNB. *Remote Sens.* **2019**, *11*, 710. [CrossRef]
29. Cao, C.; Bai, Y. Quantitative analysis of VIIRS DNB nightlight point source for light power estimation and stability monitoring. *Remote Sens.* **2014**, *6*, 11915–11935. [CrossRef]
30. Elvidge, C.D.; Baugh, K.; Zhizhin, M.; Hsu, F.C.; Ghosh, T. VIIRS night-time lights. *Int. J. Remote Sens.* **2017**, *38*, 5860–5879. [CrossRef]
31. Elvidge, C.D.; Zhizhin, M.; Ghosh, T.; Hsu, F.-C.; Taneja, J. Annual time series of global VIIRS nighttime lights derived from monthly averages: 2012 to 2019. *Remote Sens.* **2021**, *13*, 922. [CrossRef]
32. Weinold, M. A long overdue end to flicker: The 2020 EU lighting efficiency regulations. *Camb. J. Sci. Policy* **2020**, *1*, e0628620899.
33. Bullough, J.D. The blue-light hazard: A review. *J. Illum. Eng. Soc.* **2000**, *29*, 6–14. [CrossRef]
34. Bullough, J.D.; Bierman, A.; Rea, M.S. Evaluating the blue-light hazard from solid state lighting. *Int. J. Occup. Saf. Ergon.* **2019**, *25*, 311–320. [CrossRef]